Lithos 198–199 (2014) 38–57

Contents lists available at ScienceDirect

Lithos

journal homepage: www.elsevier.com/locate/lithos

Development, mobilisation and eruption of a large crystal-rich rhyolite: The Ongatiti ignimbrite, New Zealand

George F. Cooper [a,b,*], Colin J.N. Wilson [a]

[a] School of Geography, Environment and Earth Sciences, Victoria University, PO Box 600, Wellington 6140, New Zealand
[b] Department of Earth Sciences, Durham University, Science Labs, Durham DH1 3LE, UK

ARTICLE INFO

Article history:
Received 30 January 2014
Accepted 6 March 2014
Available online 25 March 2014

Keywords:
Supereruption
Ongatiti eruption
Amphibole
Trace elements
Magma chamber
Taupo Volcanic Zone

ABSTRACT

The Ongatiti ignimbrite (>~500 km^3 DRE) was erupted at 1.21 ± 0.04 Ma from the Mangakino volcanic centre (Taupo Volcanic Zone, New Zealand). The ignimbrite is crystal rich (20–30%), of rhyodacite to low-silica rhyolite composition and lacks any consistent compositional zonation. Pumice whole-rock and glass compositions and crystal rim chemistries imply that the final erupted magma body was, to a first order, homogeneous, with the only variations reflecting crystal:glass proportions in analysed clasts. Crystals from pumices can be divided into two populations based on textural and chemical signatures: those that are inferred to have grown within the final erupted magma body (82% of plagioclase, 88% of orthopyroxene, 17% of amphibole), and those that originated in a chemically heterogeneous mush zone (18% of plagioclase, 12% of orthopyroxene, 83% of amphibole). Crystal-rich microcrystalline clasts, and clots within pumices, provide direct samples of parts of this heterogeneous source region. Amphibole model temperatures and pressures, coupled with in-situ trace element concentrations suggest that the mush region extended to ~15 km depth, near the base of the quartzofeldspathic crust and was rich in amphibole. Amphibole plus subordinate plagioclase and orthopyroxene, as well as antecrystic zircon were extracted from the crystal mush and ascended to a final storage region. Model temperatures and pressures from amphibole rims and Fe–Ti oxide model temperatures imply that the final erupted magma body was stored between 770 and 840 °C at 4–6 km depths. Homogenisation of the magma body occurred through convective stirring accompanying gradually rising temperatures induced by less-evolved magma(s) emplaced at deeper levels. Plagioclase records a steady core-to-rim increase in An content, implying that a gradual heating and/or increase in H_2O in the final erupted magma body occurred over some significant period prior to the eruption. No signals of a rapid defrosting or rejuvenation event that could be considered as an eruption trigger are recorded by the crystal phases. The Ongatiti ignimbrite has features both common to, and distinct from crystal rich 'monotonous intermediates' and crystal-poor compositionally zoned rhyolites. As such, the Ongatiti ignimbrite demonstrates that 'monotonous rhyolites' can also be developed on a large scale.

1. Introduction

Models to explain the magmatic processes involved in the generation, storage and eruption of large-scale silicic magma bodies have great diversity across the realm of volcanic rocks (e.g., Hildreth, 1981). Large felsic (dacite to rhyolite) volcanic ignimbrites, particularly examples from the central USA and Andes, are commonly placed into two categories (e.g., Bachmann and Bergantz, 2008; Huber et al., 2012): the crystal-rich monotonous intermediates of broadly dacitic composition (after Hildreth, 1981) and crystal-poor, compositionally zoned rhyolites. In overall models for the generation of rhyolite melts from crystal-rich mushes (Bachmann and Bergantz, 2004; Hildreth, 2004) these two categories are interpreted, respectively, to be remobilised crystal mushes and the fractionated melt (plus entrained and newly grown crystals) that has accumulated to form a stratified melt-dominant body. However, the melt-dominant bodies for several large crystal-poor New Zealand rhyolites, although compositionally variable, were not systematically zoned (Cooper, 2014; Cooper et al., 2012; Wilson et al., 2006). In the New Zealand ignimbrite record also, there are two super-sized eruption deposits that are crystal-rich and might ostensibly be interpreted as examples of remobilised mushes. The Whakamaru deposits (Brown et al., 1998a) are inferred to represent, in large part, a crystal-rich body that was reactivated over a short (centuries to millenia) period prior to eruption (Matthews et al., 2012a,b). The Ongatiti ignimbrite from Mangakino is also crystal-rich (20–30%), of rhyodacite to low-silica rhyolite composition, and shows compositional variability, but not consistent zonation (Briggs et al., 1993). Both these deposits, however, are quartz-bearing and have higher SiO_2 contents than the examples of monotonous intermediates widely cited in the literature, such as the Fish Canyon Tuff (Bachmann

* Corresponding author. Tel.: +44 7739525205; fax: +44 0191 3342301.
E-mail address: george.cooper@durham.ac.uk (G.F. Cooper).

http://dx.doi.org/10.1016/j.lithos.2014.03.014
0024-4937/

and Dungan, 2002; Bachmann et al., 2002), Cerro Galan ignimbrite (Folkes et al., 2011; Francis et al., 1989), Atana ignimbrite (Lindsay et al., 2001) and the Lund Tuff (Maughan et al., 2002).

The question then arises as to the origins of the magma bodies that fed eruptive units like the Whakamaru and Ongatiti ignimbrites. Do they simply represent remobilised crystal mushes activated by thermal rejuvenation, but of more evolved, quartz-bearing compositions? Alternatively, do they represent erupted melt-dominant bodies that had cooled and crystallised towards, but not to the point of critical crystallinity or rheological lock-up at >~50 vol.% crystals (Brophy, 1991; Huber et al., 2010a; Marsh, 1981; Petford, 2003; Vigneresse et al., 1996)? The rapid rates of generation and 'de-generation' by crystallisation of eruptible melt-dominant bodies implied by the Oruanui (and other young eruptions at Taupo: Allan et al., 2013; Sutton et al., 2000) suggest that evolved, hot, melt-bearing mush bodies may be commonly present in silicic volcanic systems. What would such a crystal-rich rhyolitic mush look like if 'defrosted' (Mahood, 1990) or 'reactivated' (Bachmann et al., 2002; Huber et al., 2010b)?

Important clues to understanding the genesis of the New Zealand 'monotonous rhyolites' lie in the compositions and textures of crystals that reflect the processes of heating and cooling, and the records of interstitial melt compositions. Although these deposits show limited bulk compositional variations, significant variability and a complex history of open-system magmatic processes may be recorded within the mineral assemblages (e.g., Charlier et al., 2008; Matthews et al., 2012a). The addition of heat is ubiquitous in any remobilisation process, commonly inferred to be the result of underplating by less evolved to wholly mafic compositions (Bachmann and Bergantz, 2003; Bachmann et al., 2002; Couch et al., 2001; Hildreth and Wilson, 2007; Murphy et al., 2000; Pallister et al., 1992). In addition, however, that heat may be introduced with and/or by inputs of volatiles (Sisson and Bacon, 1999; the 'gas sparging' or mafic 'wind' of Bachmann and Bergantz, 2006) and/or melts of contrasting (generally less-evolved) composition. Such inputs will be reflected in changes of composition in the interstitial melts/glasses and the crystals that dissolve in, or crystallise from, those melts.

In this paper we present data from the Ongatiti ignimbrite (>500 km^3 DRE) from Mangakino volcanic centre in the Taupo Volcanic Zone (TVZ), New Zealand, to explore the processes that gave rise to this large-volume crystal-rich deposit. We evaluate the homogeneity of the Ongatiti ignimbrite through whole-rock geochemistry of juvenile clasts (pumices), and explore the development of magma system thorough the textural history and in-situ analysis of the major mineral phases. The origins of each mineral phase and the involvement of a lesser-evolved source are investigated though the study of crystals and glass in microcrystalline clots, which are commonly found within pumices and as discrete clasts. The histories of the major crystal phases are evaluated also in the light of a protracted crystallisation record in Ongatiti U–Pb zircon age spectra (Cooper et al., under review).

2. Geological background

The Taupo Volcanic Zone (TVZ) is a NNE-trending, 300 km long and up to 60 km wide region of volcanism and associated extension active since ca. 2 Ma. It forms the continental continuation of the Tonga–Kermadec arc, associated with the westward subduction of the Pacific plate beneath the Indo-Australian plate (Cole, 1990; Cole and Lewis, 1981; Gamble et al., 1996; Wilson et al., 1995). The Mangakino volcanic centre is a composite caldera structure located on and in part defining the northwestern margin of the TVZ (Fig. 1). Activity at Mangakino can be subdivided into two intense periods of large caldera-forming eruptions from 1.60 to 1.53 Ma, and 1.21 to 0.95 Ma (Houghton et al., 1995).

The Ongatiti eruption occurred at 1.21 ± 0.04 Ma (Houghton et al., 1995) producing a voluminous (>500 km^3 DRE), widespread, crystal-rich, rhyodacitic to rhyolitic ignimbrite. The ignimbrite is widely distributed to the north (as far as Auckland: Alloway et al., 2004) and west (as far as the Tasman Sea coast: Pain, 1975), and is found to the southeast at depth beneath the Waiotapu geothermal field (Wilson et al., 2010) (Fig. 1). No associated fall deposit is preserved on land, although it is represented in the deep-sea record offshore from the North Island (e.g., Allan et al., 2008).

The ignimbrite is non-welded to strongly welded, and consists of multiple flow packages, which were erupted in a series of directional lobes (Briggs et al., 1993). The deposit is subdivided into an earlier erupted facies (Eu I), and a later erupted facies (Eu II). The latter contains densely welded fragments of recycled co-eruptive vitric tuff, which are absent in the Eu I deposits (Wilson, 1986). The eruption commenced with highly energetic, violent and hotter flows, generating a pumice-poor, fine grained ignimbrite that is often strongly welded. Later flows were cooler but less energetic and less violent, generating an upper pumice-rich ignimbrite (Briggs et al., 1993; Wilson, 1986).

3. Ongatiti clast types and mineralogy

Representative juvenile clasts displaying a wide variety of textures were sampled at locations covering both the lower (Eu I) and upper (Eu II) flow packages (Fig. 1), where large pumices with low degrees of post-depositional alteration or weathering could be found.

The Eu I material was primarily sampled from Ranginui Station, ~15 km west of Mangakino township at NZMG grid reference 2738052 m E 6307658 m N. Here the ignimbrite is ~25 m thick and poorly welded, forming craggy outcrops. Sample sites for the Eu II material include Tokahaere Rock at 2735352 m E 6333586 m N, Hinuera Quarry at 2746100 m E 6361400 m N and along Horahora Road at 2743859 m E 6351620 m N, north of Mangakino, in sintered to poorly-welded ignimbrite.

3.1. Juvenile clasts

Pumice textures vary greatly throughout the ignimbrite from crystal rich and dense clasts to highly vesicular clasts with fewer crystals. Pumices from the Eu I ignimbrite are poorly to highly vesicular and crystal rich (20–30%) containing crystal schlieren, and many are flattened to fiamme. A minor proportion of crystal-moderate to crystal-rich pumices display an 'adobe-type' texture (after Hildreth and Wilson, 2007), with a coarsely fibrous lineated fabric and crystal schlieren. Pumices from the upper flows are typically crystal-moderate to -rich, with a drawn out planar fabric and an abundance of glomerocrysts. In addition to 'normal' pumices, individual clasts (up to 24 cm) of microcrystalline material occur within the upper (Eu II) ignimbrite. Greater than 50% of pumices within Eu II ignimbrite also contain clots (average size ~2 cm) of visually identical material. Both individual clasts and clots are crystal rich (20–50%) with a vesiculated glassy matrix, the crystals being almost entirely plagioclase and amphibole grains with a consistent size (~1 mm) giving the material a distinctive 'salt and pepper'-like appearance (Fig. S1).

3.2. Lithic clasts

A wide range of lithic types are found within the Ongatiti ignimbrite, including andesite and rhyolite lavas, densely welded ignimbrite (including vitric, breadcrusted recycled Ongatiti material), biotite granite and granodiorite porphyry (Brown et al., 1998b; Krippner et al., 1998). The high proportion of lava clasts suggests that the volcanic pile engulfed by the Ongatiti vents comprised significant volumes of rhyolitic and andesitic lavas from earlier effusive episodes (Krippner et al., 1998). The compositional and isotopic data from granitoid lithic fragments are similar to the range displayed in the Ongatiti ignimbrite. However, although the granitoids may be geochemically related to the Ongatiti magma, they lack any interstitial glass phase and have common

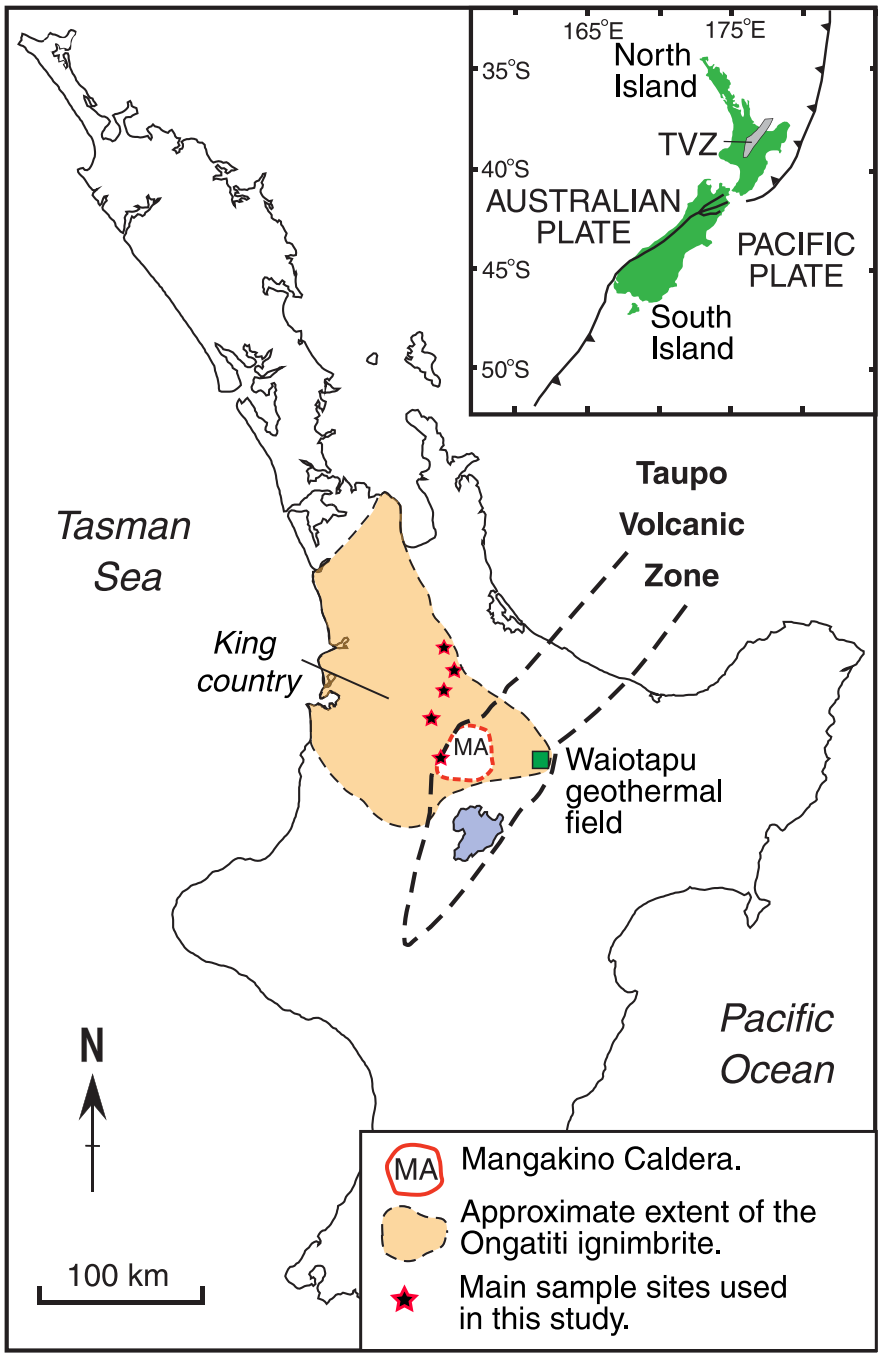

Fig. 1. Outline of the Taupo Volcanic Zone (TVZ) and its plate tectonic setting (inset), with the approximate extent of the Ongatiti ignimbrite. Modified from Briggs et al. (1993).

biotite, which is absent in the general mineral assemblage of Ongatiti pumices (Brown et al., 1998b; Krippner et al., 1998).

3.3. Mineralogy of juvenile clasts

Pumices from the Ongatiti ignimbrite contain, in general order of abundance: plagioclase, quartz, orthopyroxene, amphibole, titanomagnetite, ilmenite and accessory zircon and apatite. A number of pumices also contain sparse, light green clinopyroxene. Microcrystalline clasts and clots (abbreviated hereafter to MC) within normal pumice contain almost entirely plagioclase and amphibole grains in a highly vesiculated glassy matrix (Fig. S1). A full spectrum from plagioclase dominated (Fig. S1e) to amphibole dominated (Fig. S1h) assemblages is seen within the MC material. The plagioclase and (to a lesser extent) amphibole display a range of disequilibrium features including sieve textures, high aspect ratio skeletal grains and hopper textures (Fig. S1). Rare xenocrystic material containing a high proportion of biotite was also observed within Ongatiti pumice from the later (Eu II) material (Fig. S1a) and may represent incorporation of biotite bearing granitoid material (Krippner et al., 1998).

4. Analytical techniques

4.1. Whole rock major and trace element analyses

Whole-rock major element analysis was carried out by X-Ray Fluorescence (XRF) spectrometry using a Philips PW2400 Sequential Wavelength Dispersive X-Ray fluorescence spectrometer at the

University of Canterbury, Christchurch and a ARL 8420+ dual goniometer WDXRF spectrometer was used at CEPSAR, The Open University, UK. Loss on ignition (LOI) was determined at each institution by measuring the weight loss after heating the samples to 1000 °C for 1 h.

Whole-rock trace element analysis was carried out by solution Inductively Coupled Plasma Mass Spectrometry (ICP-MS), using an Agilent 7500cs ICP-MS at Victoria University of Wellington. Full details of sample preparation and whole rock analytical methods are in Supplementary Information and standard data are presented in Supplementary Data.

4.2. In-situ major and trace element analyses

For Electron Probe Micro-Analysis (EPMA) and Laser Ablation ICP-MS at least 25 grains of each mineral phase from each pumice sample were mounted in 32 mm wide and 5 mm thick epoxy resin blocks. Glass shards from the 250–125 μm sieve fraction were mounted into six pre-drilled holes within each epoxy block. For in-situ analysis of crystals and glass within the microcrystalline clots, a series of polished epoxy mounts were made using ~2 cm chips of this material. Back-scattered electron (BSE) imaging and quantitative major element analysis of glass and crystals were carried out using a JEOL JXA-8230

Table 1
Major (XRF) and trace element (solution-ICP-MS) whole-rock concentrations of selected pumices from the lower (EU I) and upper (EU II) parts of the Ongatiti ignimbrite.

	Eu I	Eu I	Eu I	Eu II	Eu II	Eu II	Eu II	Eu II	Eu II	Eu II	Eu II	Eu II	Eu II	BHVO-2	
Sample no.	P1991	P1992	P1994	P2027	P2018	P2023	P2028	P2026	P2024	P2019	P2021	P2022	P2025	2 s.d. %	% diff
Major elements by XRF[a]															
SiO_2	71.3	71.6	72.4	71.1	71.2	69.9	68.9	73.0	66.0	70.5	70.5	69.6	71.5	0.70	−0.3
TiO_2	0.34	0.36	0.35	0.34	0.33	0.36	0.36	0.35	0.40	0.34	0.37	0.36	0.34	1.76	−0.1
Al_2O_3	15.9	15.8	15.0	16.2	15.2	16.9	18.2	14.3	20.4	15.9	15.7	16.4	16.2	4.20	0.7
Fe_2O_3	3.16	3.52	2.86	2.75	3.05	2.75	2.76	2.89	3.77	3.12	3.51	3.64	2.07	1.23	−0.9
MnO	0.06	0.06	0.03	0.03	0.06	0.05	0.05	0.04	0.09	0.07	0.07	0.05	0.04	0.49	−0.6
MgO	0.15	0.10	0.09	0.17	0.31	0.46	0.45	0.29	0.47	0.41	0.38	0.39	0.31	2.30	0.9
CaO	1.94	1.86	1.96	2.15	2.15	2.16	2.20	1.69	2.30	2.24	2.12	2.40	2.09	0.54	−0.7
Na_2O	4.04	3.68	4.43	3.62	4.10	4.24	4.31	3.28	4.09	3.83	3.89	3.91	4.11	4.04	1.7
K_2O	2.93	2.93	2.94	3.67	3.65	3.04	2.79	4.21	2.47	3.57	3.39	3.22	3.37	5.45	1.0
LOI	1.53	2.67	1.08	1.67	1.57	3.04	2.51	1.51	4.78	1.57	2.19	3.04	2.83		
Total	99.48	99.94	99.93	99.69	99.96	99.45	99.96	98.99	99.80	99.95	99.64	99.96	99.49	0.45	−0.4
Trace elements by Solution ICP-MS															
Li	21.2	23.1	20.5	10.7	9.92	11.3	10.9	12.8	11.2	18.0	20.0	15.4	19.7	53	21
MgO	0.17	0.13	0.10	0.15	0.28	0.42	0.44	0.30	0.48	0.43	0.39	0.40	0.31	0.8	0.1
Sc	6.81	7.51	8.28	6.55	8.53	7.64	7.84	8.52	8.18	8.61	9.15	13.2	8.16	1.6	−0.3
TiO_2	0.37	0.40	0.32	0.31	0.30	0.33	0.35	0.32	0.38	0.32	0.35	0.37	0.33	13	4
V	25.4	26.2	24.7	25.9	29.0	22.3	22.0	24.5	34.9	29.3	27.9	28.4	24.9	3.5	0.9
Cr	2.13	1.76	2.19	2.97	1.75	2.12	2.22	1.86	2.44	2.87	2.26	2.13	2.45	0.9	0.05
MnO	0.06	0.06	0.03							0.07	0.06	0.05	0.04	0.6	0.01
Co	4.25	3.30	2.31	2.78	3.24	2.59	2.60	3.23	4.43	3.34	3.20	3.38	1.77	1.7	−0.2
Ni	1.59	0.89	1.07	1.05	0.73	0.89	1.00	0.90	1.36	0.93	0.88	1.17	0.71	0.9	0.2
Cu	8.68	5.95	8.94	4.35	3.77	4.50	4.45	5.81	4.05	3.48	3.03	4.14	3.30	0.9	−0.4
Zn	76.8	66.8	56.6	42.9	49.8	49.3	52.7	43.3	60.1	60.5	61.6	60.1	42.0	1.5	0.7
Ga	19.0	20.7	18.2	18.5	18.7	19.4	20.2	17.3	21.7	19.2	19.4	21.0	18.8	1.4	−0.4
Rb	94.3	94.5	94.2	81.2	87.7	85.4	83.0	104	71.3	103.6	99.4	86.7	94.6	2.3	0.7
Sr	154	150	155	155	155	163	162	119	174	169	161	186	164	2.0	0.1
Y	20.2	15.2	19.1	23.0	27.4	26.9	24.6	29.4	24.9	31.1	26.5	32.1	31.9	1.8	−0.5
Zr	90.7	74.5	65.4	91.0	101	94.0	96.4	106	103	102	106	113	98.9	1.1	−0.1
Nb	10.3	10.9	9.03	9.02	9.08	9.59	10.3	9.58	11.2	9.01	9.78	10.1	9.36	127	45
Mo	0.68	0.99	0.89	1.52	1.67	1.48	1.44	1.64	1.32	1.19	1.10	1.01	1.08	35	−13
Cs	3.53	2.55	4.36	4.89	5.62	5.40	5.72	5.93	5.68	5.95	5.47	5.98	5.55	6.0	−0.5
Ba	790	662	744	675	680	748	725	715	666	784	702	777	725	2.4	−0.4
La	24.7	19.5	27.9	19.2	25.8	25.6	21.6	24.9	23.7	27.6	24.5	43.4	34.2	2.6	−0.4
Ce	48.8	42.7	50.0	40.2	46.9	51.3	48.0	52.8	54.6	58.1	74.2	63.2	56.0	1.3	−1.3
Pr	5.83	4.51	6.86	4.47	6.93	6.20	5.05	6.17	5.37	6.86	6.03	8.30	8.28	2.2	−0.6
Nd	22.1	16.6	25.4	16.4	27.1	23.3	19.1	23.5	20.4	26.0	22.2	28.4	31.1	2.4	0.1
Sm	4.38	3.27	4.97	3.47	5.70	4.79	3.97	4.79	4.08	5.55	4.63	5.37	6.34	4.4	−0.3
Eu	0.98	0.89	1.10	0.89	1.10	1.04	0.98	0.77	1.07	1.10	1.01	1.23	1.22	1.3	0.2
Gd	4.10	3.09	4.54	3.51	5.21	4.78	3.94	4.98	4.34	5.35	4.69	5.40	6.19	1.9	0.0
Tb	0.62	0.45	0.64	0.56	0.79	0.71	0.64	0.77	0.68	0.84	0.72	0.85	0.96	2.7	−0.8
Dy	3.66	2.76	3.70	3.68	4.93	4.61	4.17	4.86	4.20	5.26	4.47	5.25	5.88	2.3	−0.4
Ho	0.73	0.55	0.70	0.78	0.97	0.95	0.84	0.99	0.84	1.09	0.94	1.09	1.17	2.4	−0.9
Er	2.12	1.63	1.97	2.31	2.86	2.84	2.58	3.00	2.61	3.24	2.74	3.18	3.39	2.3	−1.3
Tm	0.30	0.24	0.28	0.36	0.45	0.43	0.41	0.46	0.42	0.50	0.42	0.48	0.52	3.4	1.3
Yb	1.98	1.52	1.80	2.44	3.03	3.04	2.62	3.13	2.54	3.26	2.78	3.09	3.42	5.7	−0.1
Lu	0.30	0.22	0.26	0.36	0.43	0.44	0.39	0.47	0.37	0.50	0.42	0.46	0.49	5.6	−0.2
Hf	3.13	2.54	2.24	3.04	3.09	3.08	3.10	3.34	3.61	3.38	3.64	3.55	3.20	1.8	0.2
Pb	14.5	13.2	12.6	10.1	16.6	11.3	11.9	12.7	13.7	15.7	16.8	8.55	9.38	49	19
Th	11.6	10.1	9.73	9.67	12.0	10.9	11.1	11.9	11.9	11.6	12.6	13.1	11.3	2.9	0.2
U	2.05	1.72	1.47	2.04	2.37	2.29	2.36	2.61	2.09	2.60	2.29	2.39	2.43	5.2	1
Rb/Sr	0.61	0.63	0.61	0.52	0.57	0.52	0.51	0.88	0.41	0.61	0.62	0.46	0.58		
Zr/Th	7.823	7.369	6.714	9.409	8.406	8.634	8.707	8.925	8.679	8.781	8.431	8.662	8.751		
Eu/Eu*	0.70	0.86	0.71	0.78	0.62	0.66	0.76	0.48	0.78	0.61	0.66	0.70	0.59		

[a] Element oxide values are normalised to an anhydrous basis. Original LOI and Totals are given for convenience. Full standard data presented in Supplementary Data.

Superprobe at Victoria University of Wellington. Minerals were analysed with a 15 kV accelerating voltage and a 12 nA focused (~1 μm) electron beam. Glass shards were analysed with a 15 kV accelerating voltage and a beam current of 8 nA with a defocused beam (20 μm).

The trace element concentrations of minerals and matrix glass shards were determined by Laser Ablation ICP-MS using a New Wave deep ultraviolet (193 nm solid state) laser ablation system coupled to an Agilent 7500cs ICP-MS at Victoria University of Wellington. Laser ablation analysis sites within minerals were chosen on the basis of major element concentrations and zoning. The same glass shards analysed by EPMA were targeted for trace element analysis, where shard sizes permitted, major element concentrations were determined for each spot by EPMA prior to LA–ICP-MS analysis. The majority of data were acquired as static spot analyses with a beam diameter of 35 μm (reduced to 25 μm for some glass shards). Full details of in-situ analytical methods are in Supplementary Information and standard data are presented in Supplementary Data.

5. Results

5.1. Pumice whole rock compositions

Selected individual pumices covering a range of textures were chosen for whole-rock major element XRF and trace element solution ICP-MS analysis (Table 1). The majority of pumices within the Ongatiti

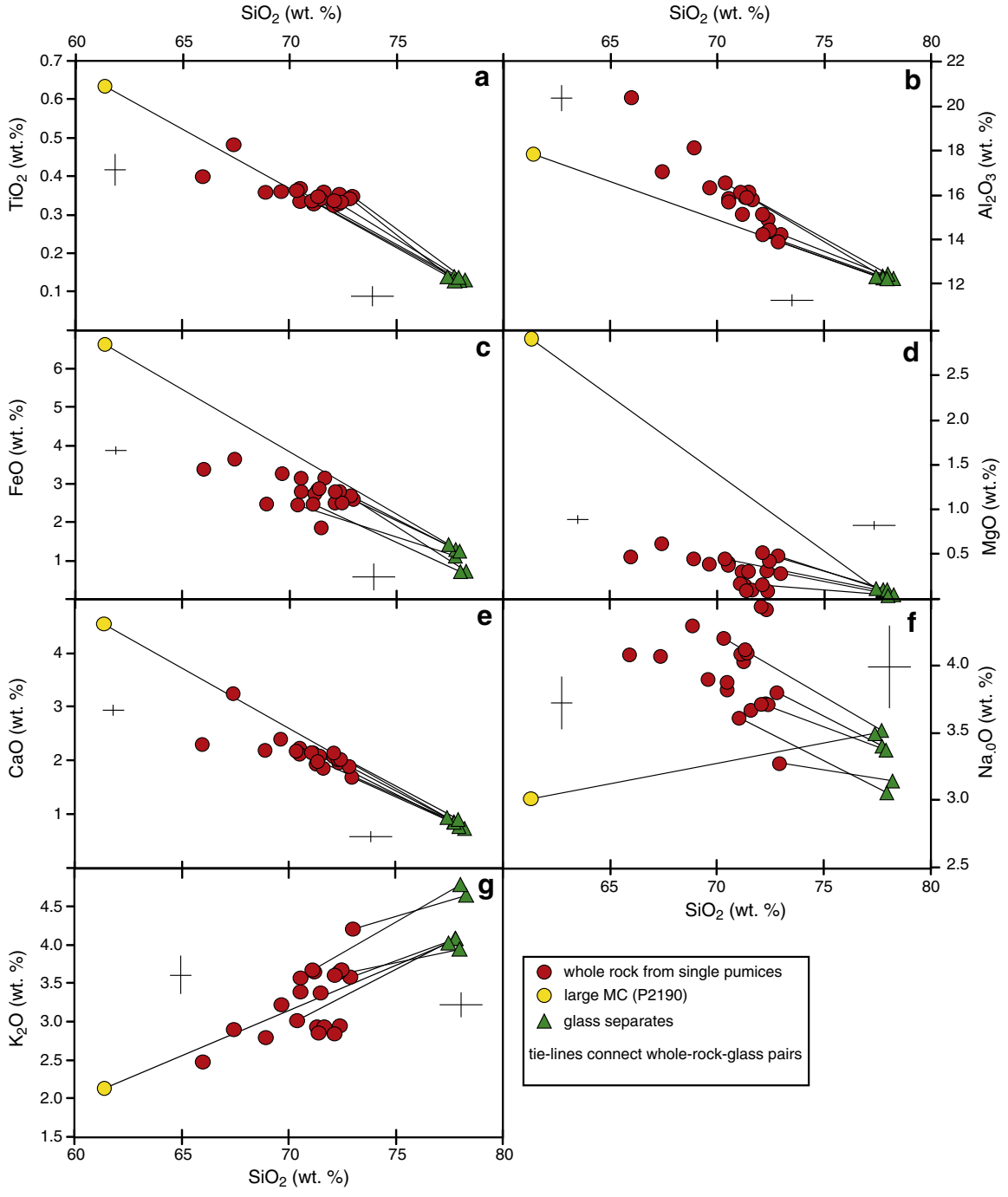

Fig. 2. Plots of major oxides versus silica for whole-rock and matrix glass for all analysed Ongatiti single pumice clasts and a large microcrystalline clot (P2190) discussed in the text. Tie lines connect whole-rock-glass pairs. Crosses represent whole-rock 2 s.d. XRF uncertainties (left hand side) and 2 s.d. EPMA matrix glass uncertainties (right hand side).

ignimbrite are rhyodacitic to rhyolitic in composition (Fig. 2). No significant differences in whole-rock major element concentrations between samples from the lower (Eu I) and upper (Eu II) ignimbrite are present (Table 1). Minor distinctions in the Zr/Th ratio are observed, which may be controlled by varying degrees of zircon crystallisation (Table 1). One large MC clast (P2190) has a less-evolved composition (Fig. 2). However, average matrix glass compositions within this sample are the same (within analytical uncertainty) as pumice matrix glass.

Average chondrite normalised rare-earth element (REE) whole-rock profiles show typical enrichments in LREE relative to HREE, but have a smaller negative Eu anomaly in comparison to typical rhyolites (Fig. 3).

5.2. Pumice matrix glass compositions

Glass within dense pumices, particularly from the lower ignimbrite (Eu I) is partially devitrified, and therefore difficult to gain reliable and meaningful chemical analyses from. Pumices from the upper ignimbrite (Eu II) containing fresh matrix glass were therefore targeted for EPMA and LA–ICP-MS analysis (Table 2). Matrix glasses from all analysed pumice samples have very similar geochemistry to each other (Fig. 4). Tie lines between major element whole rock and average matrix glass concentrations have gradients in common with the whole rock array, with the exceptions of Al_2O_3 (Fig. 2b) and Na_2O (Fig. 2f).

Compositions of pumice matrix glass are restricted with respect to the majority of trace elements, but some variations outside of analytical uncertainty are present (Fig. 4). The Rb/Sr and Eu/Eu* ratios (used as indicators of melt evolution) vary within pumice glass (Fig. 4d–f). Other trace element ratios, such as Zr/Y, Ba/La, La/Yb and Sr/Y have a very restricted range within pumice glass (Fig. 4c–e). Yb/Gd, Th and Zr concentrations, however, show ranges beyond analytical uncertainties (Fig. 4f, g). Two distinct groups based on Mn concentrations are present, at ~90–210 ppm (covarying with Mg concentrations) and ~300–320 ppm. The latter group covers a similar range in Mg as MC glasses and is at the low Mg end of the MC compositional array (Fig. 4h). The average chondrite-normalised REE matrix glass profile is similar to the whole-rock profile, but has a significantly larger negative Eu anomaly (Eu/Eu* of ~0.32).

5.3. Microcrystalline clot matrix glass

Glass within MCs has a slightly more restricted compositional range than pumice matrix glass (Fig. 4a, b). Glass within one MC (sample GC16) has a greater heterogeneity and higher SiO_2 concentrations (Fig. 4a, b). All glass analyses from each analysed pumice and MC are shown in Fig. S2. The whole rock-to-glass tie lines for a large MC clast (P2190) have similar gradients to normal pumice samples, apart from MgO (Fig. 2d) and Na_2O (Fig. 2f).

Glass trace-element concentrations within some MCs are significantly different to pumice matrix glass (Fig. 4), but one example (GC2) has indistinguishable chemistry and overlaps the pumice glass compositional range on all plots. Rb/Sr values are lower and Eu/Eu* values are higher in the other MCs (Fig. 4d, e). Trace element ratios (Zr/Y, Ba/La) are significantly elevated and span a larger range than within pumice matrix glass, but Yb/Gd covers a similar range (Fig. 4f). La/Yb and Sr/Y values extend to higher values (Fig. 4c), typical of water rich magmas in which crystallisation of plagioclase is suppressed (Chambefort et al., 2013; Richards, 2011). Higher Zr concentrations are found within the MC glasses (Table 2 and Fig. 4d) and Mg concentrations extend to much higher values than in pumice glass (Fig. 4h). In contrast to the main pumice compositional trend, Mn decreases with increasing Mg in MC glasses and there is a compositional gap between pumice and MC arrays (Fig. 4h).

Chondrite-normalised MC glass REE profiles are more depleted than pumice matrix glass (Fig. 3), particularly in MREE (Gd to Tm). Such MREE depletions are similar to those shown by andesitic REE profiles from the TVZ (Cole et al., 1983; Price et al., 2005). Europium anomalies in the MC glasses are significantly less pronounced than within pumice glasses (Fig. 3).

5.4. Pumice crystal signatures

5.4.1. Plagioclase

Plagioclase grains within pumices are up to 2.5 mm in length and are subhedral to euhedral. A dominant population (82%) of grains (Type A) have non-distinct cores, which are darker in BSE than rims. In contrast, a subordinate (Type B) population (18%) has brighter and often resorbed

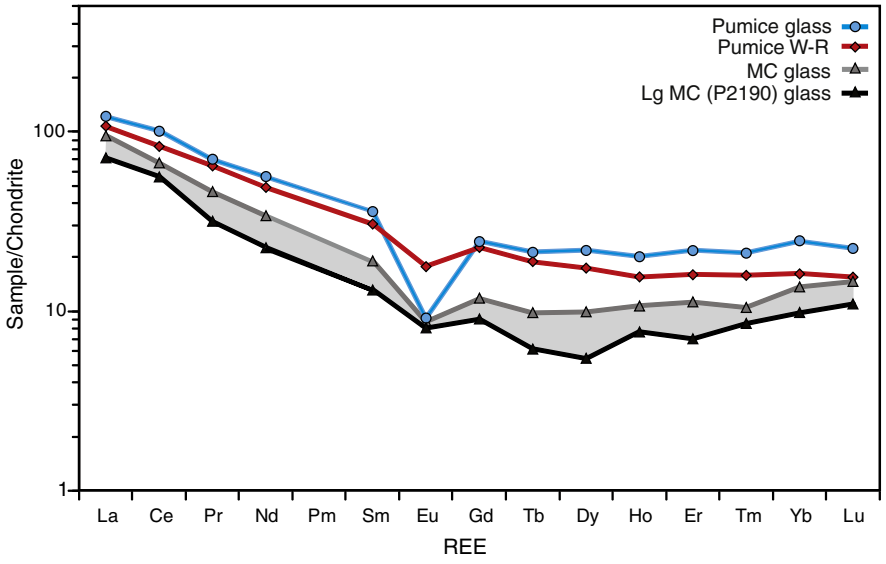

Fig. 3. Chondrite normalised Rare-Earth Element (REE) patterns for averages of pumice whole-rock, pumice matrix glass and microcrystalline clot (MC) glass. The line labelled 'large MC clast' is a single large microcrystalline clast (P2190) whereas MC glass represents an average of several smaller clasts and clots. Shaded grey area is the typical range of MC glass. Note the larger negative Eu/Eu* in pumice glass compared with whole-rock values. Chondrite normalisation values are from Evensen et al. (1978).

Table 2
Average major (EPMA) and trace element (LA–ICP-MS) concentrations of matrix glass from each analysed Ongatiti pumice and microcrystalline clast.

	Pumice glass						Microcrystalline clots										
	GC1	P2023	P2026	P2027	P2177	P2184	Lg clast P2190	Clast GC2	Clast GC10	Clast GC7	Clast GC9	Clast GC11	Clast GC16	Clot P2021	Clot P2022	ATHO-G	
																2 s.d. %	% diff
Major elements by EPMA[a]																	
SiO_2	77.7	77.7	78.2	78.0	77.9	78.6	77.4	77.6	77.6	77.5	77.8	77.7	78.6	78.0	77.8	1.2	−0.7
TiO_2	0.13	0.14	0.13	0.13	0.14	0.13	0.14	0.12	0.15	0.12	0.14	0.13	0.14	0.14	0.13	11.7	−7.6
Al_2O_3	12.3	12.4	12.3	12.5	12.3	12.2	12.4	12.4	12.3	12.4	12.2	12.3	12.4	12.2	12.3	1.3	−0.7
FeO	1.30	1.12	0.73	0.72	1.25	0.74	1.42	1.28	1.45	1.29	1.32	1.38	0.85	1.27	1.30	7.5	−2.5
MnO	0.04	0.03	0.01	0.01	0.04	0.02	0.04	0.04	0.03	0.04	0.04	0.04	0.02	0.04	0.03	23.8	−8.2
MgO	0.11	0.09	0.05	0.04	0.11	0.06	0.12	0.10	0.12	0.10	0.12	0.10	0.05	0.11	0.11	20.7	−2.8
CaO	0.85	0.86	0.74	0.77	0.91	0.79	0.94	0.85	0.94	0.85	0.90	0.84	0.87	0.94	0.90	4.3	1.1
Na_2O	3.41	3.53	3.15	3.06	3.38	3.32	3.51	3.53	3.55	3.61	3.62	3.40	3.97	3.44	3.51	5.9	−0.4
K_2O	4.08	4.08	4.65	4.79	3.94	4.09	4.02	4.03	3.89	4.08	3.83	4.13	3.13	3.88	3.90	6.5	−1.2
Total	94.8	95.2	94.9	95.4	95.2	95.7	95.2	96.1	96.1	95.7	96.7	95.1	96.3	95.8	96.3	1.1	−0.4
Trace elements by LA–ICP-MS																	
Li	35.8	50.4	58.9	48.1	43.5	47.1	28.7	44.8	36.9							31.7	20
MgO	0.13	0.11	0.07	0.12	0.13	0.08	0.20	0.13	0.19							5.9	11
CaO	0.82	0.83	0.65	0.78	0.87	0.77	0.96	0.86	0.98							13.2	−2
Sc	13.3	15.1	12.4	13.4	14.5	15.6	13.5	12.5	10.7							12.9	65
TiO_2	0.14	0.14	0.12	0.14	0.13	0.13	0.15	0.14	0.16							7.0	5
V	1.73	3.06	1.21	2.60	1.93	2.62	7.60	1.54	2.96							20.1	−17
MnO	0.04	0.02	0.02	0.02	0.04	0.02	0.04	0.04	0.04							3.8	−7
Zn	31.6	28.1	25.2	43.4	43.4	30.3	38.3	35.4	37.2							18.9	−11
Ga	15.4	15.3	15.3	18.2	14.5	15.5	17.1	15.0	15.8							20.9	−17
Rb	159	152	160	152	143	145	135	161	146							4.9	−3
Sr	53.3	53.3	49.5	49.8	54.5	54.2	71.2	54.9	62.1							5.0	−7
Y	35.8	33.5	33.4	32.2	32.1	31.5	10.0	36.5	17.6							8.7	−8
Zr	137	128	135	135	130	124	182	143	197							10.7	−4
Nb	9.15	9.44	9.04	9.60	8.69	9.60	5.95	10.02	7.18							15.7	3
Cs	7.76	7.84	8.21	8.16	7.46	8.01	7.33	8.16	7.17							15.3	−10
Ba	936	888	920	853	852	831	848	958	916							5.3	−3
La	32.1	30.2	30.4	29.6	29.3	27.5	17.5	32.3	23.2							7.9	−7
Ce	69.3	64.7	65.7	64.9	62.7	59.3	35.7	67.1	42.8							3.9	−1
Pr	7.37	7.07	6.78	7.01	6.57	6.10	3.06	7.33	4.48							6.4	−7
Nd	28.2	26.7	27.2	28.0	26.7	24.7	10.7	28.5	16.2							8.0	−4
Sm	6.37	5.22	5.94	5.00	5.17	5.09	2.02	5.91	2.94							13.4	−1
Eu	0.56	0.53	0.50	0.51	0.60	0.48	0.47	0.50	0.51							9.2	−6
Gd	5.23	4.67	5.54	4.30	5.00	4.61	1.85	5.28	2.42							11.3	−8
Tb	0.92	0.84	0.74	0.72	0.76	0.76	0.23	0.90	0.37							16.1	−9
Dy	5.54	5.01	6.09	4.90	5.07	6.01	1.39	6.18	2.52							12.5	0
Ho	1.37	1.16	1.20	1.05	1.09	1.01	0.44	1.32	0.62							13.0	−3
Er	4.06	3.60	3.70	3.50	3.23	3.52	1.17	3.96	1.87							15.6	−4
Tm	0.59	0.53	0.51	0.50	0.52	0.56	0.22	0.58	0.27							12.8	−4
Yb	4.20	4.00	4.39	3.93	3.82	3.98	1.62	4.36	2.26							11.3	−6
Lu	0.63	0.54	0.51	0.56	0.58	0.60	0.28	0.64	0.37							18.4	−5
Hf	4.19	3.89	4.38	4.00	3.91	3.89	4.24	4.45	4.97							12.3	−9
Ta	0.99	0.87	0.80	0.96	0.92	0.88	0.54	0.99	0.67							12.7	0
W	1.61	2.66	2.37	1.53	1.89	6.08	1.24	1.85	1.29							10.1	−7
Pb	21.8	16.1	17.0	14.2	20.4	17.2	16.3	19.5	19.1							16.8	−12
Th	16.9	14.7	15.5	15.0	15.0	14.1	10.9	17.1	12.6							8.7	−2
U	3.70	3.29	3.43	3.91	3.50	3.50	2.49	3.63	2.87							10.8	−6
Eu/Eu*	0.30	0.34	0.28	0.34	0.31	0.37	0.81	0.28	0.64								
Rb/Sr	3.00	2.85	3.26	3.06	2.63	2.68	1.91	2.93	2.35								

[a] Major element oxide values are normalised to 100 wt.% and totals shown are uncorrected. Representative 2 s.d. uncertainties of both techniques are presented in Supplementary Data.

cores (Fig. 5). The intermediate domains and rims of both populations typically share a common texture with fine-scale oscillatory zoning. It is important to note that both populations of grains are present in broadly similar proportions within each individual pumice from both Eu I and Eu II ignimbrite. Plagioclase cores display a large range in compositions from $An_{21–57}$ and $Or_{1.2–5.5}$, although the majority are between $An_{21–32}$ and $Or_{3.1–5.5}$ (Fig. 6) and come from the grains with non-distinct dark cores (Fig. 5). Those crystals with bright and resorbed cores (Type B) form the scatter to higher An values. Rim compositions plot within the middle of the total range of core compositions, in a tight cluster from $An_{27–33}$ and $Or_{2.9–4.0}$ (Fig. 6). Trends in trace element concentrations mirror those of the major elements (Figs. 6b & 8c). The Type A (82%) plagioclase population has small core-to-rim increases in Sr, Mn and a decrease in Ba. The Type B (18%) crystal population show the reverse of this trend with a more scattered range of core concentrations, which have lower Sr and Mn and higher Ba concentrations than corresponding rims (Fig. 6).

To explore the zoning patterns of the two plagioclase populations (Fig. 5) at a finer scale, a series of EPMA traverses were made with 15 μm spacing between analytical spots (Fig. 7a). Typically, grains with non-distinct cores and reverse zoning have a gradual rimward increase in An, with only small oscillations in An content. Grains with high An ($>An_{35}$) and often-resorbed cores display a sharp drop in composition at the core boundary, followed by a similar, progressive increase in An towards the rim (Fig. 7b).

5.4.2. Amphibole

Amphibole crystals are up to 2 mm in length, and are subhedral to euhedral. In BSE imaging 17% of amphiboles have a non-distinct core (Type A) and a higher proportion (83%) has resorbed, dark and/or

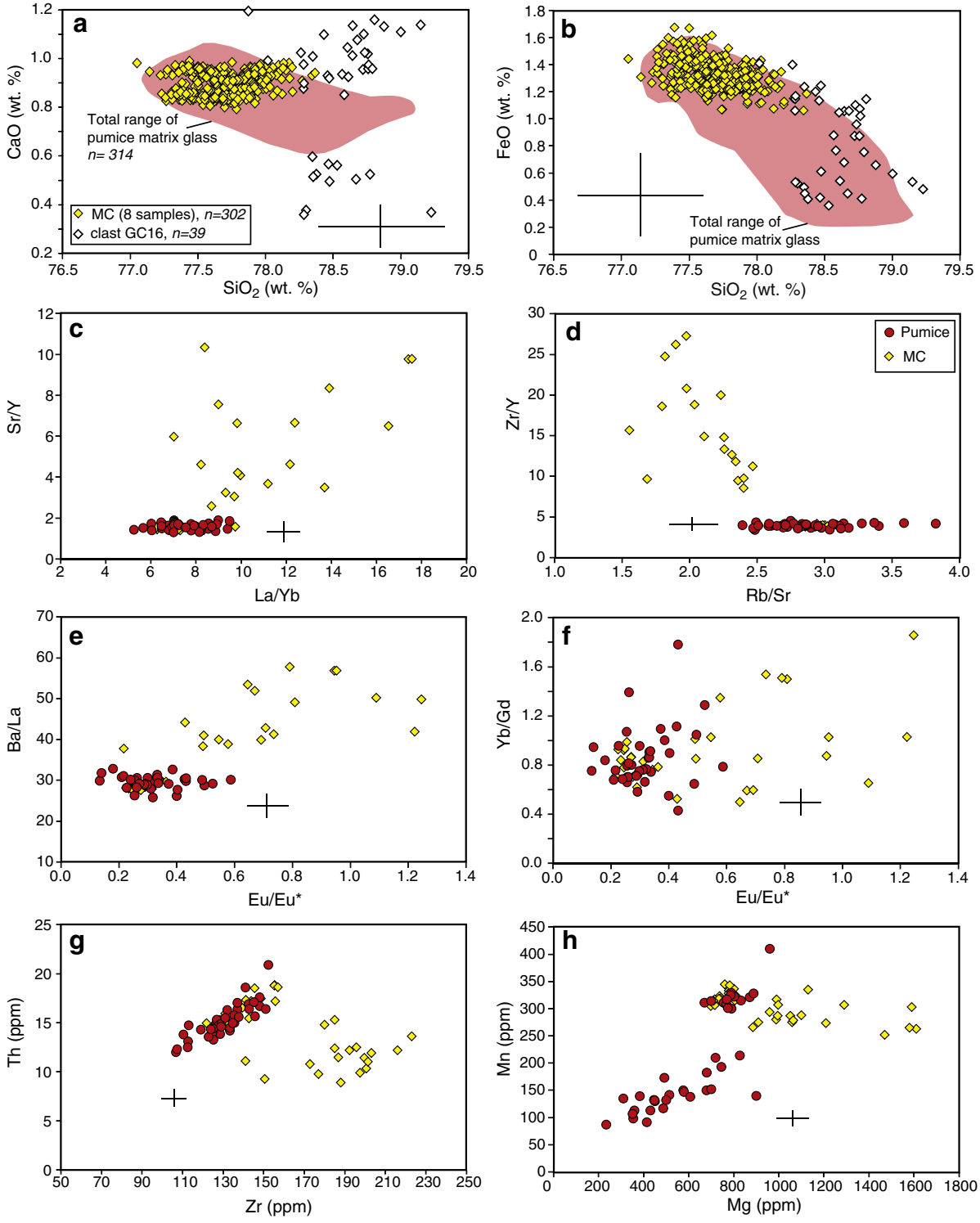

Fig. 4. SiO_2 versus CaO and FeO and selected trace element plots of matrix glass from pumice and MC fragments. Each data point represents a single analysis. Shaded areas in (a) and (b) represent compositional range of all pumice matrix glass (individual analyses from each pumice are presented in Fig. S2). Crosses represent 2 s.d. uncertainties of glass analyses, calculated from the ATHO-G standard (presented in Table 2 and Supplementary Data).

patchy cores (Type B: Fig. 5). Both crystal populations display fine-scale oscillatory zoning in their intermediate and outer zones (Fig. 5). Also, Type A and Type B amphibole populations are present in similar proportions within each pumice (as is the case for plagioclase and orthopyroxene). The majority of amphiboles found in pumices have a magnesiohornblende composition, with a lesser proportion of tschermakite–pargasite grains. Major and trace element concentrations span a significant range in amphibole cores, whereas rims have a very narrow range of compositions (Fig. 8). Core values of Al^T are spread between 1.16 and 2.10, compared to 1.20–1.42 in rims. Core values of $(Na + K)^A$ extend higher (0.27–0.69) than rims (0.27–0.49), as do $Mg/(Mg + Fe^{3+})$ values. Cores with Al^T values >1.4 (dashed line in Fig. 8) belong to the Type B population (83%) of amphiboles with dark and/or resorbed cores (Fig. 5). Trace element concentrations reveal greater compositional differences between amphibole cores and rims. A significant number of

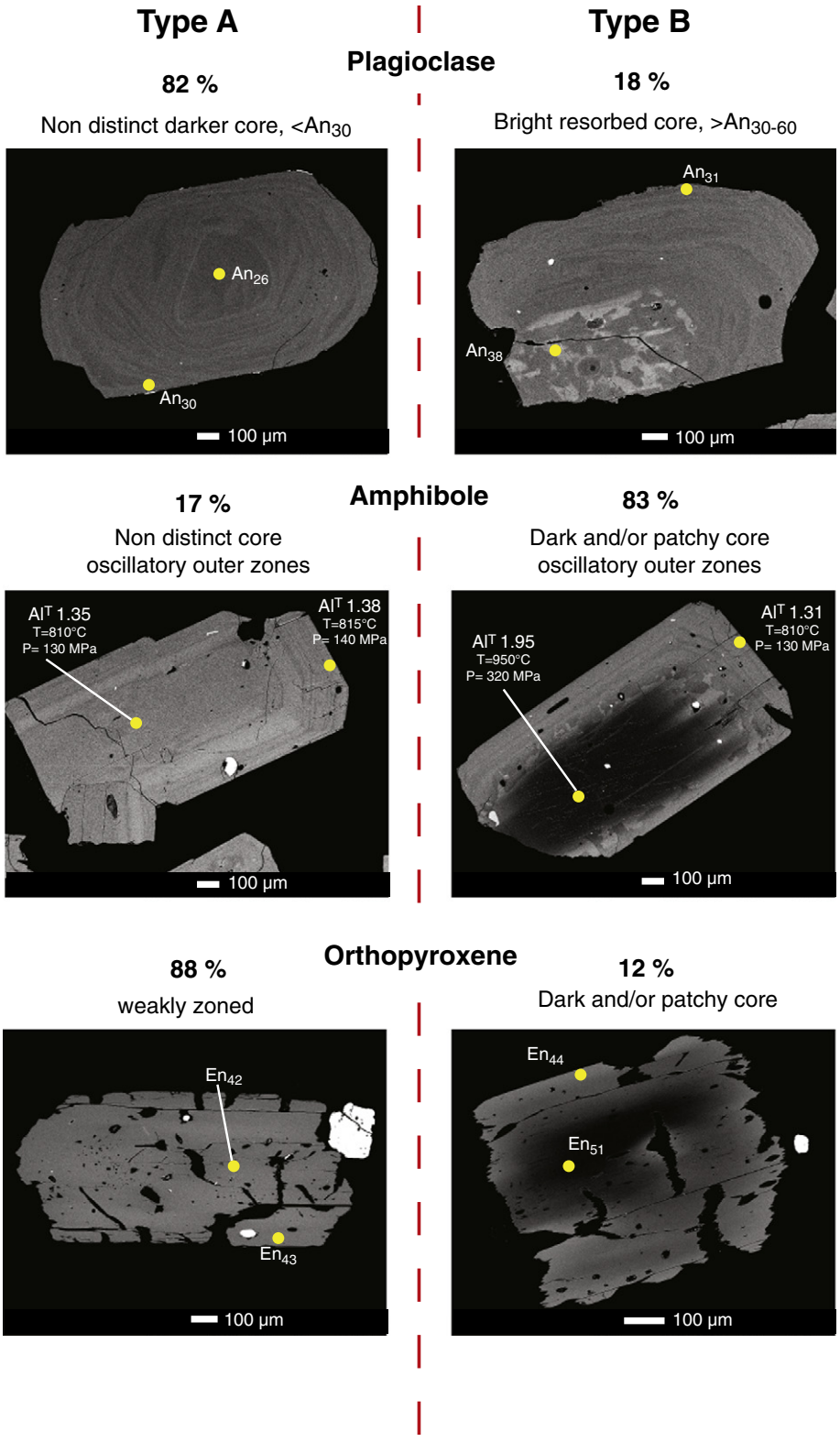

Fig. 5. Summary of textural features of Ongatiti plagioclase, amphibole and orthopyroxene. Each mineral phase is divided into two populations (Type A and B) based on core textures and chemistries (see text for details). Spots are individual representative EPMA analyses (with modelled temperatures and pressures for amphibole from Ridolfi et al., 2010).

cores have Eu/Eu* from ~0.3–0.9, and display a large range in concentrations of Sr, Ba and Mn. Values of Sr drop from ~200 to 30 ppm with decreasing Eu/Eu* ratios from ~0.9 to 0.4, whereas rims form a very tight cluster at ~30 ppm Sr and 0.15–0.20 Eu/Eu*. The array of high Eu/Eu* cores does not trend towards respective rim compositions with respect to Sr, Ba and Mn (Fig. 8). High Eu/Eu* cores have scattered Ba concentrations, whereas rims have a narrower distribution of Ba (Fig. 8d). The majority of amphiboles have lower Mn concentrations in cores than rims (Fig. 8f). Sc concentrations are low in high Eu/Eu* cores and do not change with decreasing Eu/Eu*.

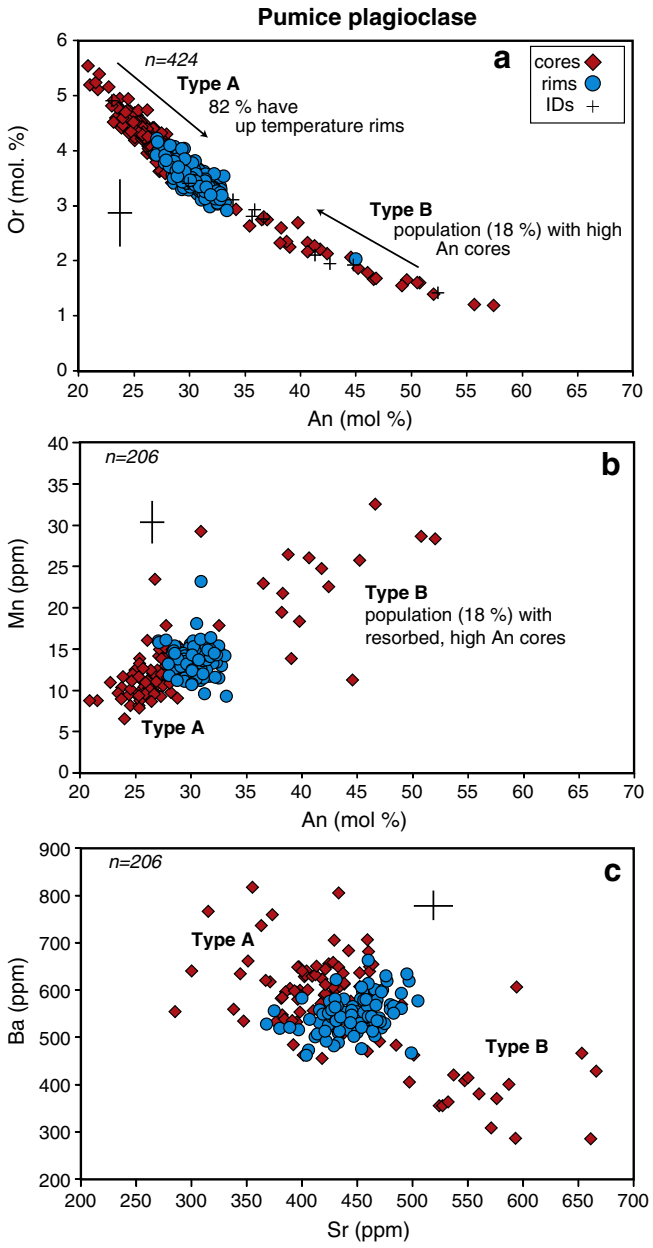

Fig. 6. Summary annotated plots of in-situ plagioclase compositions from Ongatiti pumice clasts. See text for discussion.

However, rim Sc concentrations show a large increase below ~0.3 Eu/Eu* (Fig. 8e). Cores with Eu/Eu* values >0.3 belong to the Type B (83%) amphibole population (Fig. 5), whereas at <0.3 Eu/Eu* cores are non distinct (Type A) with similar compositions to their corresponding rims.

There is a significant contrast in chondrite normalised REE profiles from amphibole cores and rims (Fig. 8). Rim profiles cover a much smaller range and are generally more enriched than cores, in which concentration ratios vary by over an order of magnitude. Rims have a very large negative Eu anomaly, whereas dark and/or patchy cores with Al^T values greater than ~1.4 (dashed line in Fig. 8) have only a small negative Eu anomaly.

5.4.3. Pyroxene

Orthopyroxene crystals (up to ~1 mm long) commonly have ragged terminations. Unlike plagioclase and amphibole, only a small proportion of orthopyroxenes have any significant zoning (Fig. 5). Orthopyroxenes can, however, still be divided into two textural populations. The dominant population (88%) displays weak zoning under BSE with slightly lighter and streaky intermediate domains (Type A), while a subordinate population (12%) has dark and/or patchy cores (Type B). Both populations are present in similar proportions within each individual pumice (as for plagioclase and amphibole). Type A orthopyroxene cores (88%) have a small compositional range and cluster at $En_{39–45}$ and $Wo_{2.1–3.4}$ (Fig. 9a) with a few scattered to higher values belonging to the 12% of grains with dark cores. Rims have a smaller range of $En_{41–45}$ and $Wo_{2.3–2.9}$ and are consistent across textural populations. Al_2O_3 concentrations are very similar between cores and rims (Fig. 9b). Ti concentrations in cores are mostly higher than in the rims (Fig. 9c). V has the largest concentration difference between cores and rims (Fig. 9d).

Rare light green clinopyroxenes, up to 1 mm in length are found within a number of pumices and are variably fractured with a ragged appearance. Cores range from $En_{26.7–33.3}$ and $Wo_{40.8–42.7}$, and rims have a narrower range from $En_{31.2–33.6}$ and $Wo_{41.7–42.8}$ (Fig. S3).

5.4.4. Fe–Ti oxides

Fe–Ti oxides within Ongatiti pumice samples are often corroded by surficial weathering, especially within the lower (Eu I) ignimbrite. Therefore only fresh samples, mainly within the upper Eu II ignimbrite, were considered reliable for in-situ analysis. Magnetite and ilmenite pairs commonly occur as inclusions within orthopyroxenes and these were targeted for analysis. Magnetite inclusions have a narrow compositional range of $Usp_{32–34}$ with a mean of Usp_{33}. Ilmenite also has a narrow compositional range, falling between $Ilm_{89–93}$ with a mean of Ilm_{90} (see Supplementary Data).

5.5. Microcrystalline clot crystal signatures

Minerals from a number of microcrystalline clasts and clots (MCs) were analysed to compare their geochemical signatures with the corresponding phases from normal pumices. Plagioclase and amphibole dominate the mineral assemblages in variable proportions within the MC material.

5.5.1. Plagioclase

Plagioclase within MCs displays a range of sizes and textures including high aspect ratio skeletal grains and hopper textures (Fig. S1; cf. Corrigan, 1982; Nelson and Montana, 1992). Plagioclase rims from small clasts and clots cover a very similar compositional range to normal pumices, clustering between $An_{29–38}$ and $Or_{2.7–3.9}$ (Fig. 10). In contrast to the Type A (82%) population of plagioclase within normal pumice, cores have higher An values than associated rims, and range between $An_{29–63}$ and $Or_{1.0–4.1}$ (Fig. 10). The dominant normal zoning in the MC plagioclase is similar to those trends seen in the Type B (18%) plagioclase population within pumices (Fig. 10).

Plagioclase from a large MC (P2190) does not display coherent zoning and is commonly recrystallised and resorbed with sieve textures, interpreted to reflect a magma mixing and/or rapid decompression event (Humphreys et al., 2006; Nelson and Montana, 1992). Grains from this MC clast (P2190) cover the same range in An as plagioclase from the other MCs, but Or values are significantly higher (~1 mol% at the same An value) (Fig. S4a), therefore forming a trend sub-parallel to the other plagioclase compositions. Mn concentrations of MC plagioclase rims are similar to rims in pumices, but cores extend to slightly higher values than the light resorbed core population (Fig. S4b). Ba and Sr rim concentrations are more variable, and cores extend to higher Sr and lower Ba than for plagioclase within pumices (Fig. S4c).

5.5.2. Amphibole

A higher number of amphiboles with tschermakite–pargasite compositions (particularly cores) are present in the MCs (see Supplementary Data). The major element chemistry of MC amphibole cores and rims shows a greater scatter than that within the felsic pumice. This is

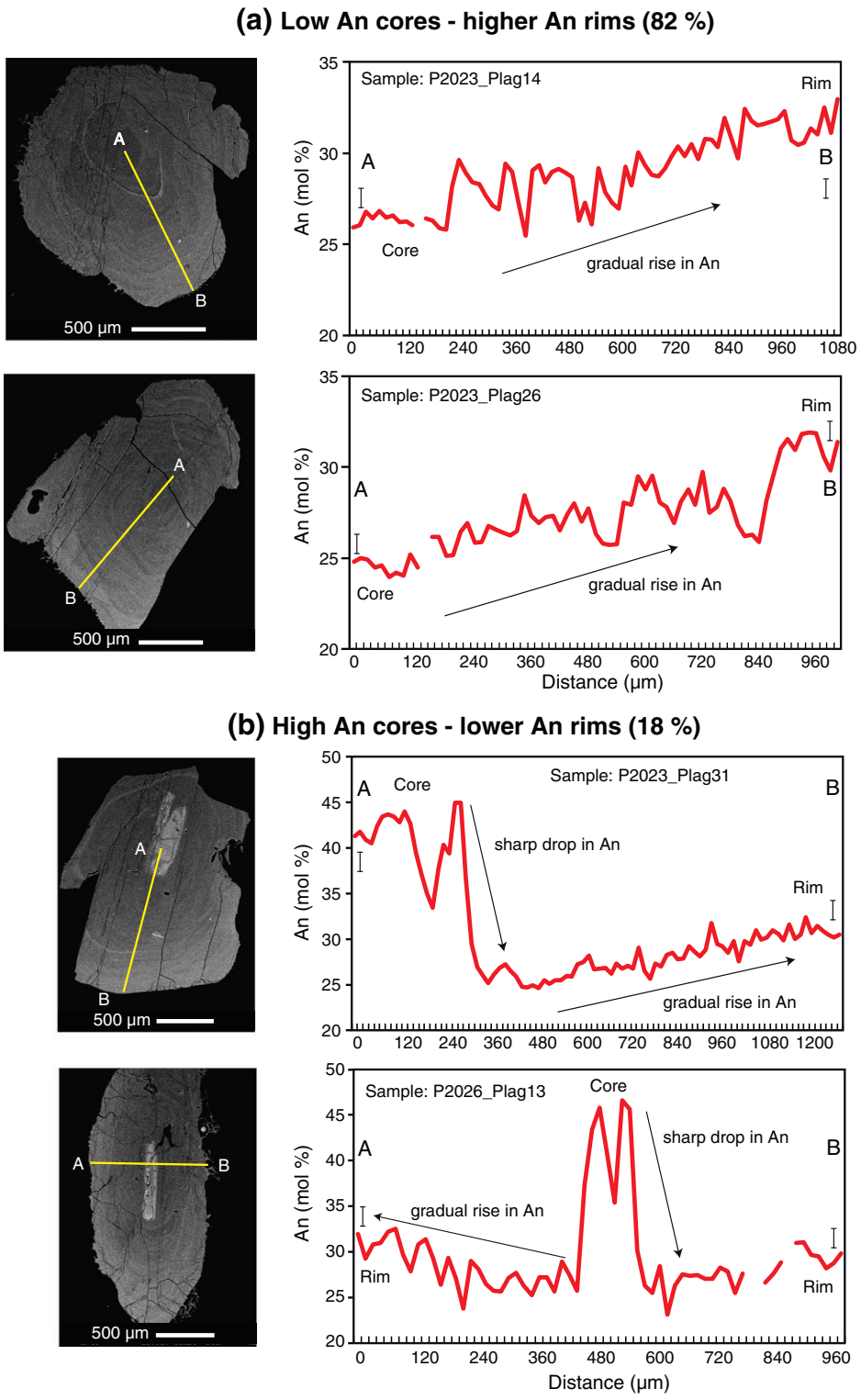

Fig. 7. Four representative core-to-rim EPMA traverses of plagioclase crystals from two Ongatiti pumices. Spot steps are at 15 µm. (a) Two profiles of plagioclase from sample P2023 with non-distinct, low-An cores demonstrating a gradual rise in An content from ~An_{25} to An_{30} from core to rim. (b) Two profiles of plagioclase from sample P2026 with bright, high An cores. The same gradual rise in An values from the outside of the core to the rim is observed.

particularly evident in plots of Al^T versus $(Na + K)^A$ and $Mg/(Mg + Fe^{3+})$ (Fig. S4d, e). Core compositions from MC amphiboles are closer in composition to Type B amphibole cores from grains within normal pumice. The majority of rims within small MCs cover a similar compositional range to those in normal pumice, with some scatter to wider compositions. As with plagioclase, many of the amphibole grains within the large MC clast (P2190) display disequilibrium textures, such as sieve textured cores. Compositional trends within amphiboles from the large MC clast (P2190) are divergent from those in normal pumice and other MCs. Cores and rims extend to higher $Mg/(Mg + Fe^{3+})$ values, and lower $(Na + K)^A$ values than amphibole cores and rims in other MCs, over a similar range in Al^T (Fig. S4d, e).

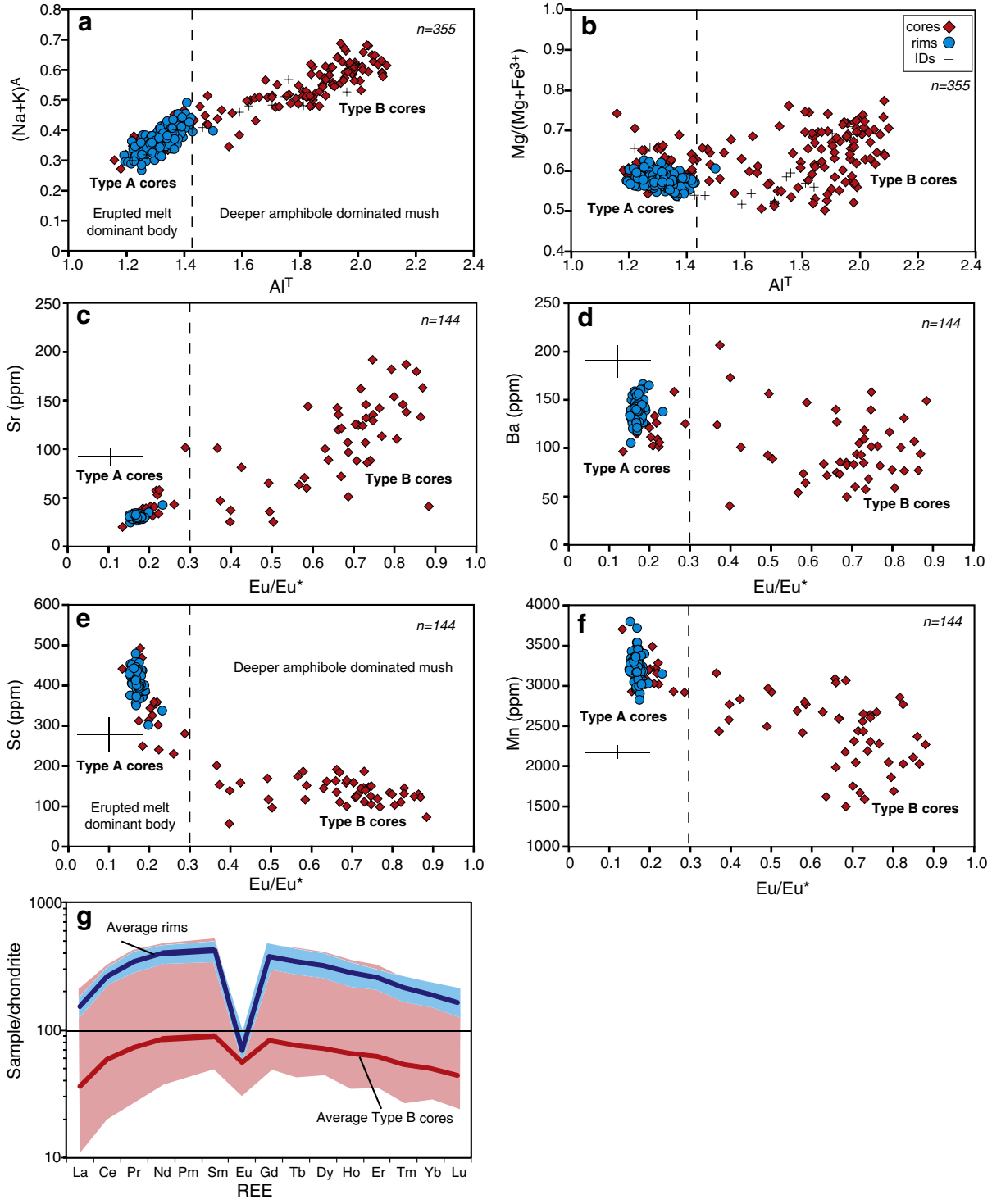

Fig. 8. In-situ major and trace element compositions of amphiboles from Ongatiti pumice clasts (a–f). In-situ, core and rim trace element concentrations in (c–f) are plotted against amphibole Eu/Eu* values, which are used as an index of evolution of the melt (low values = more evolved; high values = less evolved) at the time of crystallisation. Dashed line links the change in composition (Al^T and Eu/Eu* values) to the onset of crystallisation within the upper crustal magma body. (g) Chondrite normalised rare earth element patterns for amphiboles from pumice clasts. The blue shaded area is the total range of rim values and the blue line is the average profile. The shaded red area is the total range in core values and the red line is the average profile from cores at Eu/Eu* values of >0.4, to the right of the dashed line marked in c–f. Chondrite normalisation values are from Evensen et al. (1978).

5.6. Intensive variables

5.6.1. Fe–Ti oxide temperature and oxygen fugacity

Fe–Ti oxide magmatic model temperatures just prior to eruption were calculated using the method of Ghiorso and Evans (2008). Magnetite and ilmenite pairs included within the same host orthopyroxene were targeted to ensure textural equilibrium (Blundy et al., 2006), and all pairs were tested for equilibrium following the method of Bacon and Hirschmann (1988). In general, model temperature estimates are between 770 and 820 °C, with a mean of 790 °C. The Fe–Ti oxide

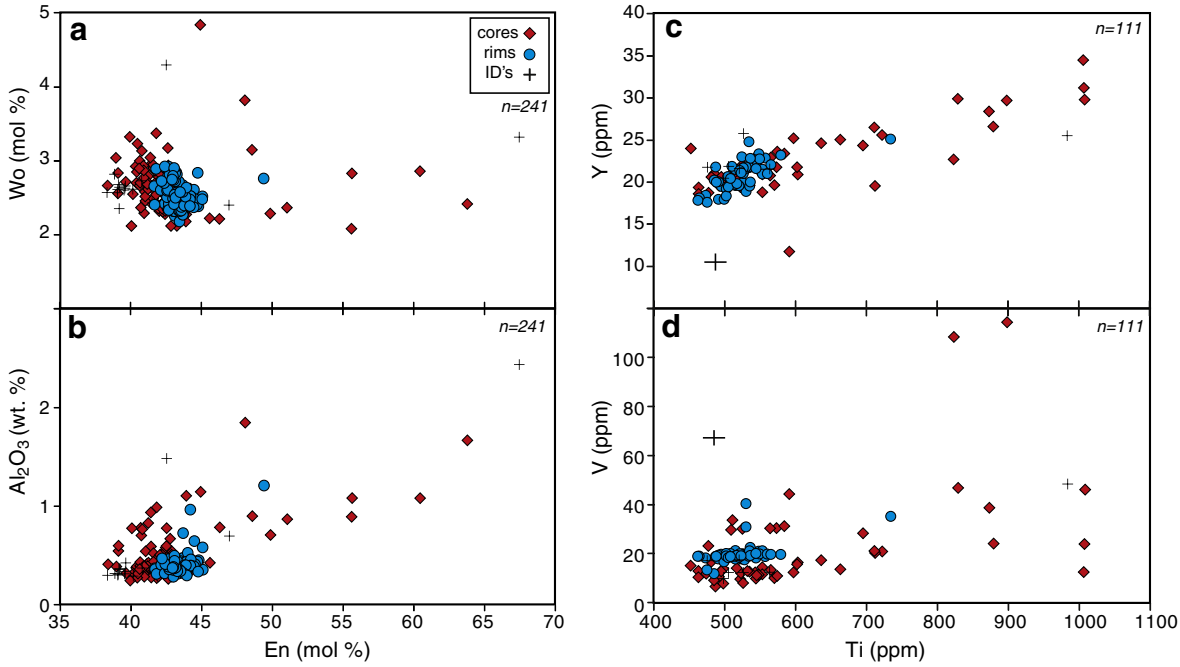

Fig. 9. In-situ major and trace compositions of orthopyroxene. Cores with compositions greater than ~En_{50} and ~600 ppm Ti are those with dark cores in BSE imagery (Fig. 5).

temperatures are the same (within uncertainty) as model temperatures from amphibole rims. Model log fO_2 estimates cover a range from −13.8 to −15.6. These temperature and oxygen fugacity estimates fall between the NNO and FMQ buffer curves (Fig. 11a).

5.6.2. Amphibole temperature and pressure

Amphiboles have the potential to record magmatic temperature and pressure changes during growth of the crystal (Johnson and Rutherford, 1989; Rutherford and Devine, 2003). Estimates of apparent temperature and pressure were made on amphiboles using the method of Ridolfi et al. (2010). Amphibole cores display a large and continuous range in apparent temperatures and pressures from 780 to 970 °C and 110 to 390 MPa (Figs. 11b and S5). Model temperatures and pressures of rims are significantly restricted in comparison, and range from 780 to 840 °C and 110 to 170 MPa (Figs. 11b and S5). These conditions correspond to model depths of amphibole core crystallisation between ~4 to 15 km and final pre-eruptive depths (crystallisation of rims) at shallower crustal levels between ~4 to 6 km (Fig. 11b).

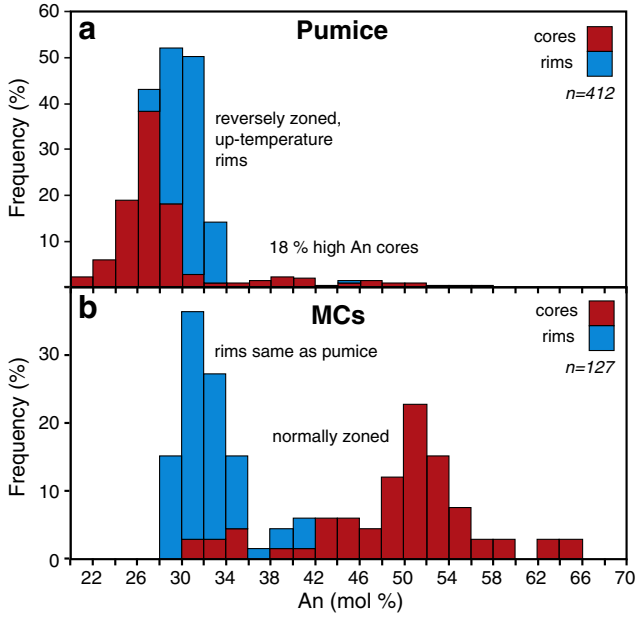

Fig. 10. Stacked histograms to summarise the contrasting compositional (An %) relationships between plagioclase cores and rims from pumice and microcrystalline clots (MCs). Frequency % values total 100% for each of the cores and rims separately.

The range in modelled pre-eruptive conditions, and the contrast in modelled pressures and temperatures between rims and cores correspond well with independently determined in-situ trace element concentrations. The lower depth of pre-eruptive conditions (~6 km) is marked by a significant change in amphibole chemistry at Al^T values of ~0.4 and Eu/Eu* of ~0.3 (dashed line in Fig. 8). The maximum estimated depth of ~15 km is consistent with the estimated depth (~16 km) of the base of the quartzo-feldspathic crust beneath much of the central TVZ (e.g., Harrison and White, 2006). The exact depth of the crust beneath Mangakino (to the north west of modelled seismic arrays) is, however, not well constrained. The validity of model amphibole temperatures and pressures was assessed using cation abundances calculated following the method of Leake et al. (2004). Evidence for both temperature (edenite and Ti-Tschermak) and pressure (Al-tschermak) sensitive atomic substitution mechanisms are found across the whole amphibole dataset (cf. Bachmann and Dungan, 2002; De Angelis et al., 2013) (Fig. S6). Amphibole rims show little or no correlations between cation abundances due to the consistency of amphibole rim concentrations (i.e. no significant variations in model temperature and pressure estimates). Average pre-eruptive temperature estimates from amphibole rims are within uncertainty of the model temperatures estimated from Fe–Ti oxides (Fig. 11). Higher temperature (870–970 °C) crystals with dark and/or patchy cores yield higher estimations of melt H_2O (~6 wt.%) compared to ~5 wt.% in lower temperature cores and rims.

Amphibole cores from individual MCs record similar model temperature (780–950 °C) and pressure ranges (110–410 MPa) to their counterparts from pumices (Figs. 11c and S5). Amphibole rims cover a larger range in model temperatures (790–910 °C) and pressures (120–320 MPa) than rims in normal pumice (Figs. 11c and S5). Amphiboles from these MCs show evidence for temperature exchange (edenite and Ti-tschermak) and, but to a lesser extent pressure (Al-tschermak) sensitive atomic substitution mechanisms (Fig. S6). Amphiboles from the large MC clast (P2190) show less evidence for temperature (edenite

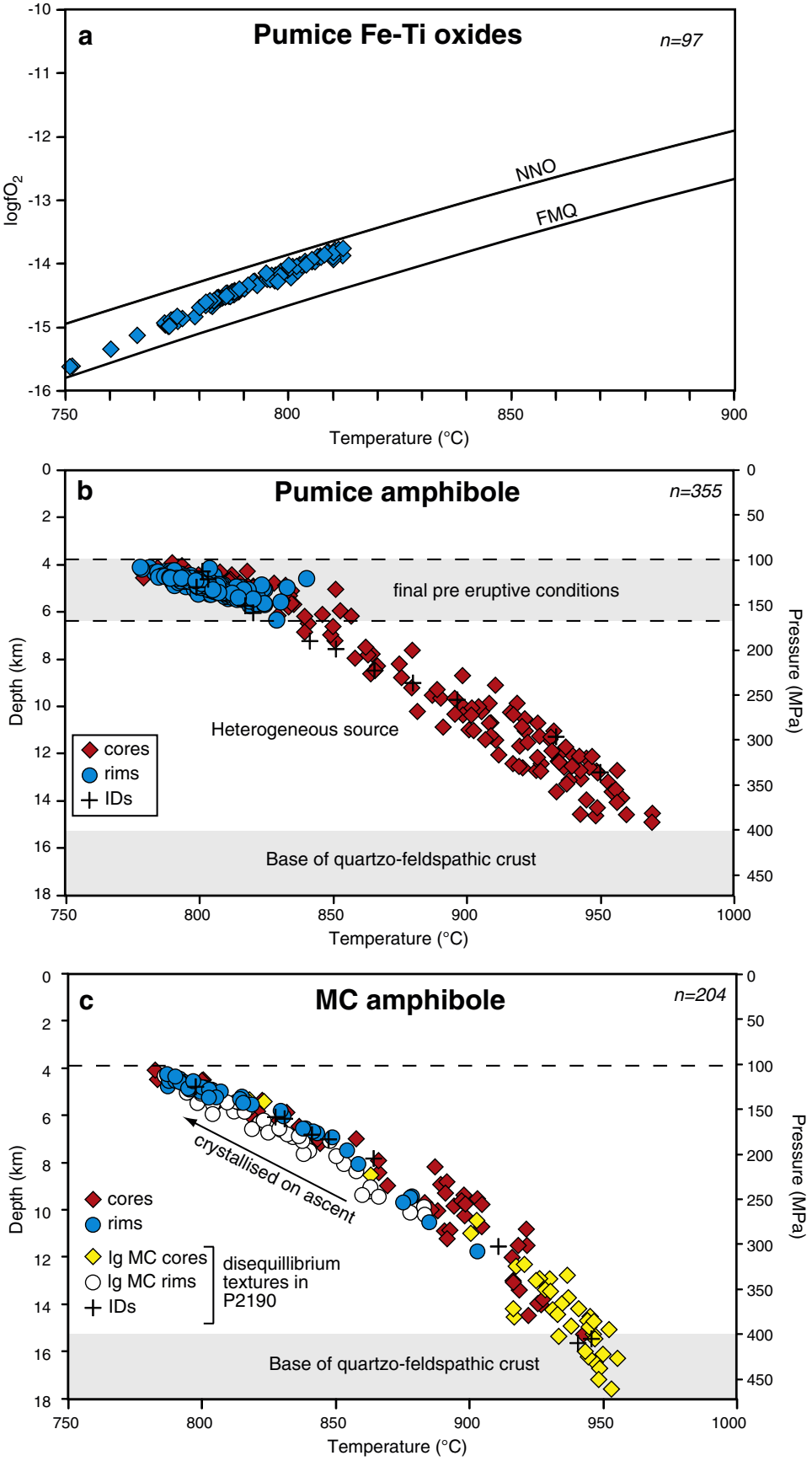

Fig. 11. (a) Fe–Ti oxide model temperatures and oxygen fugacites calculated using the methods of Ghiorso and Evans (2008). (b & c) Model temperatures (°C), pressures (MPa) and estimated depths for amphibole cores, intermediate domains and rims from pumices (b) and microcrystalline clasts (c) calculated using the methods of Ridolfi et al. (2010). Dashed shaded area represents the inferred depths at which rims crystallised and amphibole was stored prior to eruption.

and Ti-tschermak) and pressure (Al-tschermak) sensitive atomic substitution mechanisms (Fig. S6). Also, many amphibole grains from sample P2190 display disequilibrium textures and therefore the reliability of any thermobarometry estimates are compromised in this case. Model melt H_2O concentrations extend to higher water contents within the large MC clast (5–8%) and are close to the limit of amphibole stability, which in turn may account for the observed disequilibrium textures.

6. Discussion

6.1. Origin of textural and chemical signatures in the Ongatiti crystals

To a first order, the Ongatiti ignimbrite is relatively homogeneous, with restricted ranges in both whole-rock and glass compositions and no significant compositional gradients between pumices from the earlier versus later flows. There is a larger range in whole rock pumice compositions than in the associated matrix glass, which can be considered homogeneous within the uncertainties of the analytical technique (Fig. 2). Due to the crystal-rich nature of pumices, the range in whole-rock compositions is thus interpreted to be entirely a reflection of the crystal assemblage and crystallinity of each individual pumice. In contrast to this large-scale homogeneity, the textural and chemical variations within individual crystals (particularly plagioclase and amphibole) record contrasting early growth histories, which suggest that open system processes in a dynamic magmatic system operated.

Based on textural and chemical signatures in the crystals, the mineral assemblages of the final erupted magma volume can be divided into two distinct populations. The first population (Type A) is inferred to have grown in-situ in the melt-dominant body (Fig. 12) and is represented by grains with non distinct cores [82% (plagioclase) 88% (orthopyroxene), 17% (amphibole) of the respective crystal populations: Fig. 5]. The second population (Type B) [18% (plagioclase) 12% (orthopyroxene), 83% (amphibole) of the respective crystal populations: Fig. 5] contains less-evolved cores that are inferred to have been sourced from the deeper crystal mush (Fig. 12). The crystallisation of amphibole and subordinate plagioclase and orthopyroxene within a deeper crystal mush probably accompanied a major crystallisation event, peaking at 1.30–1.32 Ma, recorded in zircons (Cooper et al., under review). We therefore infer that the majority of zircons are antecrystic, inherited from the deeper source zone (Fig. 12). Only a limited proportion of zircons grew within the pre-eruptive melt-dominant magma body at shallower levels (Fig. 12). The composition of the melt, and pre-eruptive model temperatures from both amphibole and Fe–Ti oxides (total range of ~770–840 °C) imply that the final erupted magma body was in a condition just above zircon saturation (Boehnke et al., 2013; Hanchar and Watson, 2003). Under these conditions, the antecrystic zircon population would not be rapidly dissolved, but significant in-situ crystallisation of zircon within the magma body would be limited (cf. Charlier et al., 2005).

6.1.1. Plagioclase

The dominance (82%; Type A) of plagioclase with non-distinct, low-An cores is attributed to crystallisation entirely within the evolved crystal-rich, but melt-dominant body (Fig. 12). Ongatiti plagioclase, which dominates the mineral assemblage (70–90%), therefore mostly records processes and changing magmatic conditions within the upper, more evolved portion of the magmatic system (Fig. 12). The subordinate (18%; Type B) plagioclase population with higher An cores suggests an input of crystals grown in lesser-evolved melt, and/or at conditions of higher magmatic temperatures and water contents (Fig. 12), when compared to the final erupted magma body. Core-to-rim plagioclase traverses show that all plagioclase crystals share a common history from the core-rim boundary to their outer rims (Fig. 5), implying that antecrystic higher-An plagioclase grains were entrained with rising melt and incorporated within the developing melt-dominant body (Fig. 12). Resorption of these cores, giving rise to their patchy appearance, is likely to have occurred during ascent (Humphreys et al., 2006). Plagioclase compositions are controlled by temperature, pressure, and melt composition coupled with a major dependence on H_2O content (Housh and Luhr, 1991; Lange et al., 2009; Putirka, 2005, 2008; Rutherford and Devine, 1988). A consistent and gradual core-to-rim reverse zoning trend from An_{25} to An_{30} therefore indicates a progressive change in one or more of these parameters during crystallisation. Results from crystallisation experiments of A-type granites by Klimm et al. (2003) show that at temperatures of 800 °C a rise from An_{25} to An_{30} requires a temperature increase of ~50 °C or an increase in melt H_2O of ~0.5 wt.%. These melt changes could be invoked by underplating of the crystal-rich mush by a less-evolved melt, with the potential to increase temperature and change melt chemistry and volatile content (increase in Ca and H_2O) (Bachmann and Bergantz, 2006; Bachmann et al., 2002). It is likely, however, that a ~50 °C increase in temperature acting in isolation would be texturally and/or chemically recorded within the other crystal phases, in particular amphibole and orthopyroxene. Type A amphiboles, however, display little or no evidence for core-rim increases in model temperatures (maximum ~20 °C: Fig. S5). Therefore, in addition to temperature, the gradual rise in plagioclase An is considered to have been influenced by an increase in the H_2O content (and other volatiles) of the melt during crystallisation.

6.1.2. Amphibole

The dominance of amphiboles with patchy and/or resorbed (83%; Type B) cores displaying a large range in major and trace element chemistries implies that there is a significant contribution of crystals from a source that was chemically variable (but overall less-evolved than the final erupted magma) and may have spanned a large range of temperatures, pressures and depths. Amphiboles therefore have the potential to yield information on a crystal mush source that is not recorded in the dominant Type A plagioclase population, grown within the final erupted magma body. Eu/Eu* values and Sr concentrations in Type B cores are higher and more variable than in overgrowth rims suggesting that significantly lower degrees of plagioclase crystallisation had occurred in the melt from which amphibole cores grew when compared with the final pre-eruptive melt.

A significant shift in the chemistry of amphiboles is recorded at ~1.4 Al^T and ~0.3 Eu/Eu*, which is inferred to mark the point at which amphibole began to accumulate around 4–6 km depth and began crystallising alongside dominant plagioclase. Amphibole compositions less than ~1.4 Al^T and ~0.3 Eu/Eu* correspond to a period of stable growth of intermediate domains and rims, which have oscillatory zoned textures. The similarities between oscillatory zoned plagioclase and amphibole suggest that both phases record a common history in their later stages of growth (Fig. 12). The significant addition of amphibole to the final erupted magma body from depth must therefore have occurred during its early development, accompanying ascent of the subordinate population of plagioclase with resorbed cores, minor orthopyroxene with higher Mg cores and incorporation of the dominant zircon population with its ~1.3 Ma crystallisation peak (Cooper et al., under review).

6.1.3. Orthopyroxene

Orthopyroxenes within the Ongatiti system lack the complex crystallisation record preserved in plagioclase and amphiboles. Any oscillatory zonation may have been lost over time through Fe–Mg interdiffusion. Only 12% of grains (Type B; dark, high En cores) show any significant shifts in chemistry implying that the majority of crystals (with weak zoning) crystallised under conditions similar to those just prior to eruption. Therefore it is inferred that Type A (88%: Fig. 5) orthopyroxene grew alongside Type A plagioclase for its entire history and was not sourced to any significant extent from the amphibole dominated mush zone.

6.2. Origin of microcrystalline clots

From their less-evolved compositions, crystal-rich natures and presence as clots in pumices, the MCs are interpreted as samples of the mid-crustal source region of the Ongatiti magmatic system from where the Type B (82%) amphiboles originated. As the MC material is present both as individual clasts and as clots within pumices, and with no evidence for compositional gradients due to mixing, it can be inferred that limited mingling with the final erupted magma occurred (cf. Blake et al., 1992). There is a general absence of MCs within the Eu I pumices, and therefore it is inferred that the introduction of the MCs into the discharging material occurred during later stages of the eruption.

Glass compositions within all but one MC (sample GC16) are indistinguishable in terms of major elements but significantly more depleted in REE than pumice glass. The disparity in the MC glasses between their high silica rhyolite major element compositions (77.5–79 wt.% SiO_2), and their less-evolved trace element signatures, is likely controlled by late-stage rapid crystallisation from a melt close to its eutectic. The REE patterns of MCs have a closer resemblance to those of whole-rock andesite than those of rhyolite. The REE concentrations are variable between MCs and may suggest a source with variable melt chemistries and/or variable proportions of crystallisation of the mineral assemblage (Fig. 12). Variable melt chemistries recorded in individual MCs may arise due to boundary layer concentration gradients during the rapid quenching and crystallisation of lesser evolved melt emplaced into the rhyolite melt (Albarede and Bottinga, 1972; Faure and Schiano, 2005). Therefore, melt compositions that do not follow a typical liquid line of descent may be present due to these local melt disequilibria. The MCs may be analogous to the crystal rich andesitic clasts erupted during the ~330 ka Matahina eruption, Okataina volcanic complex, TVZ which are interpreted to represent samples of an intermediate crystal mush (Deering, 2009; Deering et al., 2011). A considerably smaller Eu/Eu* anomaly implies that this melt is less evolved and has undergone less plagioclase crystallisation than glass in the pumices (Fig. 3). Higher Sr/Y, La/Yb and Ba/La ratios of MC glass (Fig. 4) further suggest lesser

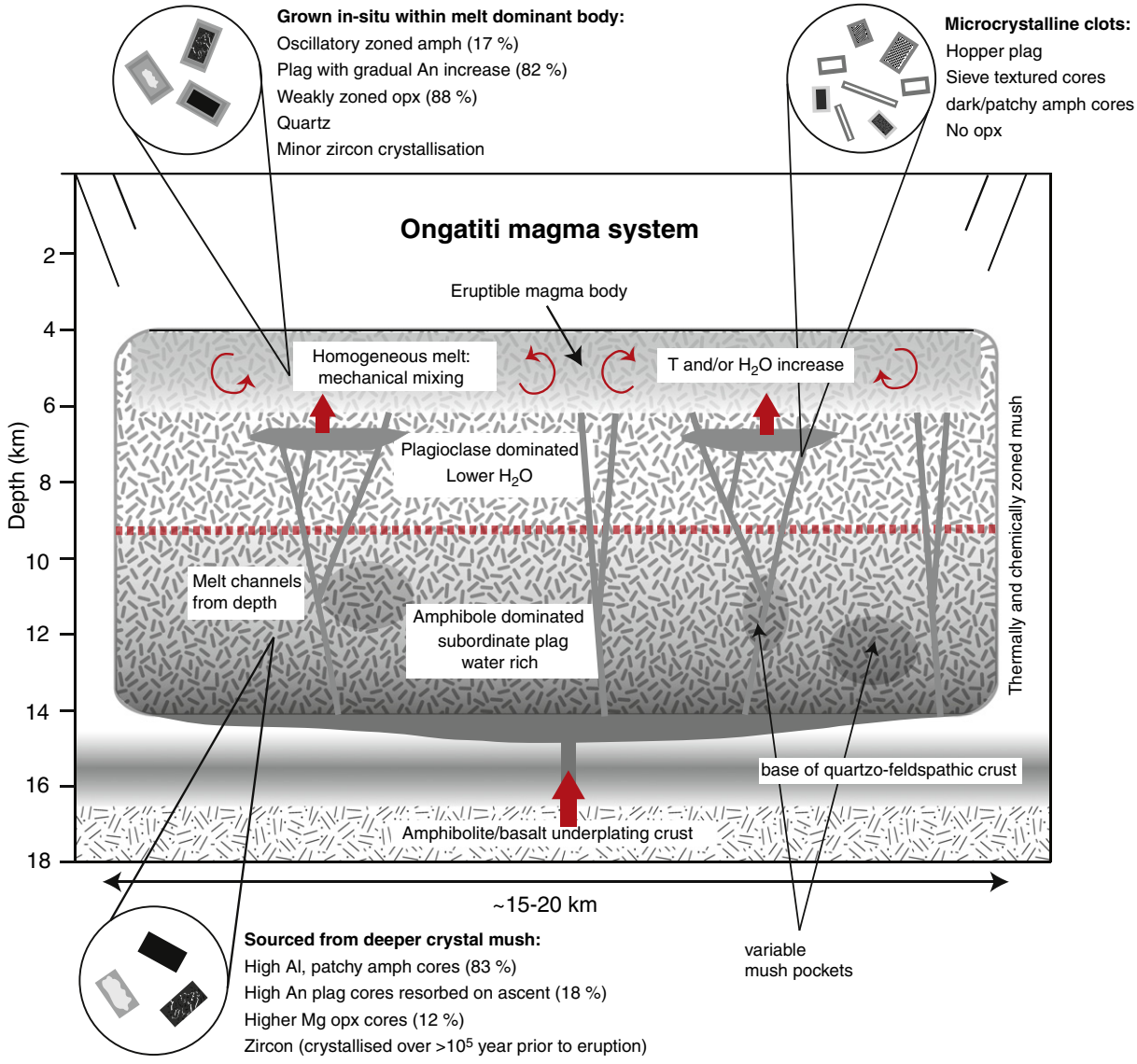

Fig. 12. Semi quantitative cross section of the Ongatiti magma system. The origin and formation of plagioclase and amphibole zoning populations (see Fig. 5) within pumices, and the microcrystalline clots are shown. The dashed red line marks an approximate change from an amphibole dominated source to plagioclase dominated assemblages at shallower levels. Pervasive melt channels are inferred to be present which allow for the rapid ascent of crystals and melt (forming microcrystalline clots) from depth. Depths are estimated from amphibole compositions using the method of Ridolfi et al. (2010). The horizontal extent of the system is approximate, but scaled to be consistent with the overall volume of the Ongatiti eruption deposits. See text for discussion.

degrees of plagioclase crystallisation, which were suppressed by high water contents (Chambefort et al., 2013; Richards, 2011). These observations are consistent with the signals recorded in high Al amphibole cores (Type B) within pumices (Fig. 8), providing further support for a water rich zone that has undergone less plagioclase crystallisation. The Yb/Gd ratio covers the same range as within pumices, suggesting that significant crystallisation of amphibole (relatively enriched in MREE/HREE: Sisson, 1994) had already taken place from the lesser-evolved melt, and provides further evidence for an source/mush zone with high water contents (cf. Deering, 2009; Deering et al., 2011). Mn concentrations of MC glass are higher than within pumice and increase with decreasing Mg concentrations (Fig. 4g). This trend may be explained by a lack of crystallising orthopyroxene within the source/mush, or the breakdown of orthopyroxene (which is highly enriched in Mn), alongside significant amphibole crystallisation (removing Mg from the melt). Higher Zr concentrations within MC glass (Fig. 6a, e) suggest lesser degrees of zircon crystallisation within this melt.

The crystal assemblage of the MCs is entirely plagioclase and amphibole, with accessory Fe–Ti oxides. Amphiboles within the MC clasts (excluding P2190) have cores with a very similar range of chemistry and modelled temperatures and pressures as the patchy cored amphiboles (Type B) in pumices, implying that they may have originated from a common source under similar magmatic conditions. In addition, the majority of MC plagioclase cores span the same range in An values as the resorbed plagioclase cores (Type B) in pumices, providing further evidence for a common source region (Fig. 12). The lack of orthopyroxene within MCs supports the glass Mg versus Mn trends and implies that either no significant orthopyroxene crystallisation occurred at depth, or extensive and complete orthopyroxene breakdown occurred during ascent (cf. Allan et al., 2013), consistent with the nature of the high En orthopyroxene cores (Type B: 12%) within pumices. A range of disequilibrium textures (sieve textures, high aspect ratio skeletal grains and hopper grains) is displayed by plagioclase, and to a lesser extent amphibole in the MC clasts. These textures are likely caused by rapid decompression, loss of H_2O during ascent and/or cooling upon engulfment in the final erupted magma (Humphreys et al., 2006; Nelson and Montana, 1992).

6.3. The role of crystal mush in the development of the Ongatiti system

Briggs et al. (1993) suggested that the variation in pumice chemistry found throughout the Ongatiti ignimbrite implied that the magma body was originally stratified, but that this stratification was lost just prior to, or during eruption. Although a stratified magma chamber could explain the trends observed in whole rock chemistry, explaining the textural and chemical signatures of the crystal populations seen in pumices with this model is problematic. If a chemically stratified magma body was present, it is likely that the outer zones of crystals would have correspondingly different chemistries, recording the varying pre-eruptive magmatic conditions. However, the crystal rims within all crystal phases, from the full textural range of pumices analysed show very little compositional variability and suggest that the final erupted magma body was generally homogeneous. The Ongatiti U–Pb zircon age spectra indicate a protracted growth history, spanning ~250 kyr, and peaking in abundance around ~100 kyr prior to the nominal eruption age (Cooper et al., under review). Maintaining a large melt-dominant body under uniform conditions for periods of the order of 10^5 years is inherently problematic, requiring very well balanced influxes of heat and mass (e.g., Mahood, 1990; Sparks et al., 1990). The zircon age record coupled with the diversity in crystal core compositions supports the notion of a large crystal-rich (mush) body with subordinate melt that was present for the $1–2 \times 10^5$ year period prior to eruption.

Within the Ongatiti magma system, model temperatures and pressures from high-Al cored amphiboles suggest that a thermally and chemically variable crystal mush/source may have reached to depths close to the base of the quartzofeldspathic crust (~15 km). Controversies about the role of melt chemisty, H_2O and fO_2 in influencing model temperatures and pressures yielded by the single-phase model of Ridolfi et al. (2010) may mean that some values are unrealistic (e.g., Coombs et al., 2013, citing Browne, 2005). In addition to evidence of temperature and pressure controlled cation exchange in amphibole (Fig. S6), three factors suggest that the model figures may be valid to a first order. First, at all stages the amphiboles appear to have co-crystallised with plagioclase, so ensuring that Al contents in the melt were buffered. Second, the use of other Al-in-amphibole barometers also yield pressures broadly consistent with those from the formulation of Ridolfi et al. (2010). Third, the Ongatiti ignimbrite contains scarce lithic fragments of basement schist (Krippner et al., 1998), in addition to the low-grade greywacke metasediment (which is ubiquitous in New Zealand ignimbrites), suggesting that deeper crustal levels (>~ 10 km) were being excavated (cf. Mortimer, 2000). The extraction of crystals from an amphibole bearing mush at mid-crustal depths has also been suggested in the case of the Matahina eruption (Deering, 2009; Deering et al., 2011).

6.4. Heterogeneity to homogeneity in the Ongatiti magma body

The textural and compositional signatures from crystal cores in Ongatiti pumices suggest that a relatively evolved and uniform melt-dominant magma body was assembled at shallow levels from a large and diverse source region from variable depths in the crust (Fig. 12). In turn, crystal rim compositions and the similarity of glass chemistries between pumices imply that the final erupted volume of melt was effectively homogeneous. The homogenisation of crystal-rich magma bodies is thought to arise through: (1) the addition of magma similar in composition to that of the growing reservoir, (2) significant mechanical mixing and/or convective stirring, (3) the hindering of crystal-melt separation or latent heat buffering (Bachmann and Bergantz, 2008; Huber et al., 2009). The data presented here demonstrates that both open and closed system processes were involved in the accumulation and homogenisation of the Ongatiti melt-dominant magma body.

Although the Type B crystal cores in pumices display evidence for a heterogeneous source/mush and earlier growth at variable depths and conditions, this was followed by a period of crystallisation at shallow crustal levels (4–6 km) prior to eruption (Fig. 12). The Type A crystals are interpreted to have entirely crystallised at shallow crustal levels, coevally with the rims on Type B crystals. Crystallisation during this period of shallow accumulation did not accompany significant cooling within the magma body and it did not approach a state where a crystal framework was formed. The outermost rims of all crystal phases are either the same or slightly less evolved than interiors and all plagioclase crystals have a gradual up-temperature (and/or H_2O content) signal (Fig. 7), suggesting that the shallow magma body had relatively uniform or slightly increasing temperatures during crystallisation (cf. Bachmann, 2010), possibly in part balanced by latent heat release of crystallisation. Contrasts between the prominent negative Eu anomaly in pumice matrix glass versus significantly smaller values for the whole-rock negative Eu anomaly (Fig. 3) are explicable by nearly all plagioclase growing in the shallow magma body remaining suspended in the melt from which it crystallised. The Ongatiti situation contrasts markedly with that in the 25.4 Oruanui magma system, where the (rapidly accumulated) melt-dominant body cooled by about 50 °C over the short (centuries) period between when melts were introduced from the underlying mush and the magma body destroyed on eruption (Allan et al., 2013). We do not have any constraints on the timescale of crystallisation during rising temperatures and/or increases in H_2O from the initial assembly of the melt dominant body to eruption. Recent studies show that the rejuvenation of crystal mushes in large silicic systems may occur over an extended period of time (e.g., the Fish Canyon Tuff: Wotzlaw et al., 2013). Alternatively the mobilisation of crystals from a mush and storage in a melt dominant body may be a rapid process (Allan et al., 2013; Cooper and Kent, 2014).

Conditions within the final erupted Ongatiti magma body may also reflect heat inputs from continued underplating of less evolved magma within the crystal mush. The MCs are interpreted to be the crystallised representatives of this magma, and aspects of their chemistry suggest that it was of broadly andesitic composition and water-rich (possibly saturated). The underplated magma is inferred to have provided a source of heat and volatiles, which could have contributed to convection and mixing within the final erupted magma body to contribute to its overall homogeneity (Bachmann and Bergantz, 2006; Couch et al., 2001; Rutherford and Devine, 2003). The consistent oscillatory zonation recorded in plagioclase and amphibole may therefore reflect this convection. The absence of significant steps in mineral compositions and lack of disequilibrium textures suggest that the involvement of any underplated magma was gradual, and did not occur as a distinct rejuvenation event (Couch et al., 2001; Murphy et al., 2000). In contrast, plagioclase and amphibole from the Fish Canyon Tuff typically display large spikes in elemental concentrations reflecting their inferred up-temperature evolution as a result of a series of rejuvenation events (Bachmann and Dungan, 2002; Bachmann et al., 2002). Apart from the syn-eruptive incorporation of MCs, there is no evidence for the mixing of magmas with different compositions prior to eruption, on a scale that would cause significant shifts in chemistry of the melt and evidence for dissolution of crystals (cf. Bachmann et al., 2002).

7. Conclusions

Crystals from pumices in the Ongatiti ignimbrite record a complex history, providing evidence for the establishment of a crystal-rich (but melt-dominant), homogeneous rhyolite magma body from a chemically heterogeneous source extending to depths approaching the base of the quartzofeldspathic crust. The Ongatiti ignimbrite does not conform to either the crystal-rich 'monotonous intermediates' or the crystal-poor compositionally zoned rhyolites and demonstrates that large-silicic magma systems can develop in a different fashion, that of 'monotonous rhyolites'. The generation of the Ongatiti magmatic system can be explained through the following processes:

1. During a period from 1.32 to 1.30 Ma (Cooper et al., under review), the majority of zircons now found in Ongatiti pumices crystallised within a chemically variable, amphibole rich mush zone at depths of up to 15 km. These antecrystic zircons, along with amphibole and subordinate plagioclase and orthopyroxene, were extracted from the crystal mush and ascended to final storage in a plagioclase dominated upper zone at depths between 4 and 6 km (Fig. 12). The majority of plagioclase, and nearly all orthopyroxene were lost by dissolution through decompression melting during ascent. In contrast, the majority of high-Al amphibole cores and zircons survived. The contrast between crystals that survived ascent to form cores in Type B crystals, versus those (Type A) that grew in the shallow, melt-dominant body, give rise to the contrasting textural and chemical record of crystal populations within Ongatiti pumices.
2. The melt-dominant Ongatiti magma body accumulated at depths of between 4 and 6 km over some period prior to eruption. Significant crystallisation of plagioclase, alongside, quartz, orthopyroxene, amphibole and only limited zircon occurred at these depths. During this stage the magma body was essentially a closed system, as little fractionation or removal of crystals (no crystal-melt separation), and no significant mixing with magmas of contrasting compositions occurred.
3. As crystallisation of the shallow-level body continued, homogenisation of the magma body occurred through convective stirring, accompanying gradually rising temperatures and/or water contents inferred to have been induced by continued injection of less-evolved magma (represented by the microcrystalline clots) into the underlying crystal-rich root zone. The increasing H_2O and temperature of the melt is recorded by gradual increases in plagioclase An content (An_{25-30}). Underplating of the less evolved, water rich magmas transferred volatiles, particularly H_2O, to the high-level magma body without any physical exchange of melt and crystals. The final erupted magma body, although crystal-rich, remained melt dominated by and did not approach a state of 'lock-up'. No signals of a sharply defined 'defrosting' or 'rejuvenation' event are recorded in the Ongatiti pumices.

Supplementary data to this article can be found online at http://dx.doi.org/10.1016/j.lithos.2014.03.014.

Acknowledgements

We thank Victoria University for a PhD Scholarship for GFC, and the Royal Society of New Zealand for the support from the Marsden Fund (VUW0813) and for a James Cook Fellowship for CJNW. We also thank John Watson at the Open University and Stephen Brown at the University of Canterbury for XRF analyses, and Marc-Alban Millet and Joel Baker for their support and discussions in the laboratory work. The manuscript highly benefited from comments made by Olivier Bachmann, Sarah Henton De Angelis and Andrew Kerr.

References

Albarede, F., Bottinga, Y., 1972. Kinetic disequilibrium in trace element partitioning between phenocrysts and host lava. Geochimica et Cosmochimica Acta 36, 141–156.
Allan, A.S.R., Baker, J.A., Carter, L., Wysoczanski, R.J., 2008. Reconstructing the Quaternary evolution of the world's most active silicic volcanic system: insights from an 1.65 Ma deep ocean tephra record sourced from Taupo Volcanic Zone, New Zealand. Quaternary Science Reviews 27, 2341–2360.
Allan, A.S.R., Morgan, D.J., Wilson, C.J.N., Millet, M.-A., 2013. From mush to eruption in centuries: assembly of the super-sized Oruanui magma body. Contributions to Mineralogy and Petrology 166, 143–164.
Alloway, B., Westgate, J., Pillans, B., Pearce, N., Newnham, R., Byrami, M., Aarburg, S., 2004. Stratigraphy, age and correlation of middle Pleistocene silicic tephras in the Auckland region, New Zealand: a prolific distal record of Taupo Volcanic Zone volcanism. New Zealand Journal of Geology and Geophysics 47, 447–479.
Bachmann, O., 2010. The petrologic evolution and pre-eruptive conditions of the rhyolitic Kos Plateau Tuff (Aegean Arc). Central European Journal of Geosciences 2, 270–305.
Bachmann, O., Bergantz, G.W., 2003. Rejuvenation of the Fish Canyon magma body: a window into the evolution of large-volume silicic magma systems. Geology 31, 789–792.
Bachmann, O., Bergantz, G.W., 2004. On the origin of crystal-poor rhyolites: extracted from batholithic crystal mushes. Journal of Petrology 45, 1565–1582.
Bachmann, O., Bergantz, G.W., 2006. Gas percolation in upper-crustal silicic mushes as a mechanism for upward heat advection and rejuvenation of near-solidus magma bodies. Journal of Volcanology and Geothermal Research 149, 85–102.
Bachmann, O., Bergantz, G.W., 2008. Rhyolites and their source mushes across tectonic settings. Journal of Petrology 49, 2277–2285.
Bachmann, O., Dungan, M.A., 2002. Temperature-induced Al-zoning in hornblendes of the Fish Canyon magma, Colorado. American Mineralogist 87, 1062–1076.
Bachmann, O., Dungan, M.A., Lipman, P.W., 2002. The Fish Canyon magma body, San Juan volcanic field, Colorado: rejuvenation and eruption of an upper-crustal batholith. Journal of Petrology 43, 1469–1503.
Bacon, C.R., Hirschmann, M.M., 1988. Mg/Mn partitioning as a test for equilibrium between coexisting Fe–Ti oxides. American Mineralogist 73, 57–61.
Blake, S., Wilson, C.J.N., Smith, I.E.M., Walker, G.P.L., 1992. Petrology and dynamics of the Waimihia mixed magma eruption, Taupo Volcano, New Zealand. Journal of the Geological Society, London 149, 193–207.
Blundy, J., Cashman, K., Humphreys, M., 2006. Magma heating by decompression-driven crystallization beneath andesite volcanoes. Nature 443, 76–80.
Boehnke, P., Watson, E.B., Trail, D., Harrison, T.M., Schmitt, A.K., 2013. Zircon saturation re-revisited. Chemical Geology 351, 324–334.
Briggs, R.M., Gifford, M.G., Moyle, A.R., Taylor, S.R., Norman, M.D., Houghton, B.F., Wilson, C.J.N., 1993. Geochemical zoning and eruptive mixing in ignimbrites from Mangakino volcano, Taupo Volcanic Zone, New Zealand. Journal of Volcanology and Geothermal Research 56, 175–203.
Brophy, J.G., 1991. Compositional gaps, critical crystallinity, and fractional crystallization in orogenic (calc-alkaline) magmatic systems. Contributions to Mineralogy and Petrology 109, 173–182.
Brown, S.J.A., Wilson, C.J.N., Cole, J.W., Wooden, J., 1998a. The Whakamaru group ignimbrites, Taupo Volcanic Zone, New Zealand: evidence for reverse tapping of a zoned silicic magma system. Journal of Volcanology and Geothermal Research 84, 1–37.
Brown, S.J.A., Burt, R.M., Cole, J.W., Krippner, S.J.P., Price, R.C., Cartwright, I., 1998b. Plutonic lithics in ignimbrites of Taupo Volcanic Zone, New Zealand: sources and conditions of crystallisation. Chemical Geology 148, 21–41.
Browne, B.L., 2005. Petrologic and Experimental Constraints on Magma Mingling and Ascent: Examples from Japan and Alaska. Ph.D. thesis University of Alaska, Fairbanks.

Chambefort, I., Dilles, J.H., Longo, A.A., 2013. Amphibole geochemistry of the Yanacocha Volcanics, Peru: evidence for diverse sources of magmatic volatiles related to gold ores. Journal of Petrology 54, 1017–1046.
Charlier, B.L.A., Wilson, C.J.N., Lowenstern, J.B., Blake, S., van Calsteren, P.W., Davidson, J.P., 2005. Magma generation at a large, hyperactive silicic volcano (Taupo, New Zealand) revealed by U–Th and U–Pb systematics in zircons. Journal of Petrology 46, 3–32.
Charlier, B.L.A., Wilson, C.J.N., Davidson, J.P., 2008. Rapid open-system assembly of a large silicic magma body: time-resolved evidence from cored plagioclase crystals in the Oruanui eruption deposits, New Zealand. Contributions to Mineralogy and Petrology 156, 799–813.
Cole, J.W., 1990. Structural control and origin of volcanism in the Taupo Volcanic Zone, New Zealand. Bulletin of Volcanology 52, 445–459.
Cole, J.W., Lewis, K.B., 1981. Evolution of the Taupo–Hikurangi subduction system. Tectonophysics 72, 1–21.
Cole, J.W., Cashman, K.V., Rankin, P.C., 1983. Rare-earth element geochemistry and the origin of andesites and basalts of the Taupo Volcanic Zone, New Zealand. Chemical Geology 38, 255–274.
Coombs, M.L., Sisson, T.W., Bleick, H.A., Henton, S.M., Nye, C.J., Payne, A.L., Cameron, C.E., Larsen, J.F., Wallace, K.L., Bull, K.F., 2013. Andesites of the 2009 eruption of Redoubt volcano, Alaska. Journal of Volcanology and Geothermal Research 259, 349–372.
Cooper, G.F., 2014. The Dynamics of Large-scale Silicic Magmatic Systems: Case Studies from Mangakino Volcanic Centre, Taupo Volcanic Zone, New Zealand. Ph.D. thesis Victoria University, Wellington, New Zealand.
Cooper, K.M., Kent, A.J.R., 2014. Rapid remobilization of magmatic crystals kept in cold storage. Nature 506, 480–483.
Cooper, G.F., Wilson, C.J.N., Millet, M.-A., Baker, J.A., Smith, E.G.C., 2012. Systematic tapping of independent magma chambers during the 1 Ma Kidnappers supereruption. Earth and Planetary Science Letters 213-214, 23–33.
Cooper, G.F., Wilson, C.J.N., Charlier, B.L.A., Wooden, J.L., Ireland, T.R., 2014. Temporal evolution and compositional signatures of two supervolcanic systems recorded in zircons from Mangakino volcanic centre. New Zealand. Contributions to Mineralogy and Petrology (under review).
Corrigan, G., 1982. The crystal morphology of plagioclase feldspar produced during isothermal supercooling and constant rate cooling experiments. Mineralogical Magazine 46, 433–439.
Couch, S., Sparks, R.S.J., Carroll, M.R., 2001. Mineral disequilibrium in lavas explained by convective self mixing in open magma chambers. Nature 411, 1037–1039.
De Angelis, S.H., Larsen, J., Coombs, M., 2013. Pre-eruptive magmatic conditions at Augustine Volcano, Alaska, 2006: evidence from amphibole geochemistry and textures. Journal of Petrology 54, 1939–1961.
Deering, C.D., 2009. Cannibalization of an amphibole-rich endesitic progenitor induced by caldera collapse during the Matahina eruption: evidence from amphibole compositions. American Mineralogist 94, 1162–1174.
Deering, C.D., Cole, J.W., Vogel, T.A., 2011. Extraction of crystal-poor rhyolite from a hornblende-bearing intermediate mush: a case study of the caldera-forming Matahina eruption, Okataina volcanic complex. Contributions to Mineralogy and Petrology 161, 129–151.
Evensen, N.M., Hamilton, P.J., O'Nions, R.K., 1978. Rare-earth abundances in chondritic meteorites. Geochimica et Cosmochimica Acta 42, 1199–1212.
Faure, F., Schiano, P., 2005. Experimental investigation of equilibration conditions during forsterite growth and melt inclusion formation. Earth and Planetary Science Letters 236, 882–898.
Folkes, C.B., de Silva, S.L., Wright, H.M.N., Cas, R.A.F., 2011. Geochemical homogeneity of a long-lived, large silicic system; evidence from the Cerro Galán caldera, NW Argentina. Bulletin of Volcanology 73, 1455–1486.
Francis, P.W., Sparks, R.S.J., Hawkesworth, C.J., Thorpe, R.S., Pyle, D.M., Tait, S.R., Mantovani, M.S., McDermott, F., 1989. Petrology and geochemistry of volcanic rocks of the Cerro Galan caldera, northwest Argentina. Geological Magazine 126, 515–547.
Gamble, J.A., Woodhead, J.D., Wright, I.C., Smith, I.E.M., 1996. Basalt and sediment geochemistry and magma petrogenesis in a transect from oceanic island arc to rifted continental margin arc: the Kermadec–Hikurangi margin, SW Pacific. Journal of Petrology 37, 1523–1546.
Ghiorso, M.S., Evans, B.W., 2008. Thermodynamics of rhombohedral oxide solid solutions and a revision of the Fe–Ti two-oxide geothermometer and oxygen-barometer. American Journal of Science 308, 957–1039.
Hanchar, J.M., Watson, E.B., 2003. Zircon saturation thermometry. Reviews in Mineralogy and Geochemistry 53, 89–112.
Harrison, A., White, R.S., 2006. Lithospheric structure of an active backarc basin: the Taupo Volcanic Zone, New Zealand. Geophysical Journal International 167, 968–990.
Hildreth, W., 1981. Gradients in silicic magma chambers: implications for lithospheric magmatism. Journal of Geophysical Research 86, 10153–10192.
Hildreth, W., 2004. Volcanological perspectives on Long Valley, Mammoth Mountain, and Mono Craters: several contiguous but discrete systems. Journal of Volcanology and Geothermal Research 136, 169–198.
Hildreth, W., Wilson, C.J.N., 2007. Compositional zoning of the Bishop Tuff. Journal of Petrology 48, 951–999.
Houghton, B.F., Wilson, C.J.N., McWilliams, M.O., Lanphere, M.A., Weaver, S.D., Briggs, R.M., Pringle, M.S., 1995. Chronology and dynamics of a large silicic magmatic system: central Taupo Volcanic Zone, New Zealand. Geology 23, 13–16.
Housh, T.B., Luhr, J.F., 1991. Plagioclase-melt equilibria in hydrous systems. American Mineralogist 76, 477–492.
Huber, C., Bachmann, O., Manga, M., 2009. Homogenization processes in silicic magma chambers by stirring and mushification (latent heat buffering). Earth and Planetary Science Letters 283, 38–47.
Huber, C., Bachmann, O., Dufek, J., 2010a. The limitations of melting on the reactivation of silicic mushes. Journal of Volcanology and Geothermal Research 195, 97–105.
Huber, C., Bachmann, O., Manga, M., 2010b. Two competing effects of volatiles on heat transfer in crystal-rich magmas: thermal insulation vs defrosting. Journal of Petrology 51, 847–867.
Huber, C., Bachmann, O., Dufek, J., 2012. Crystal-poor versus crystal-rich ignimbrites: a competition between stirring and reactivation. Geology 40, 115–118.
Humphreys, M.C., Blundy, J.D., Sparks, R.S.J., 2006. Magma evolution and open-system processes at Shiveluch Volcano: insights from phenocryst zoning. Journal of Petrology 47, 2303–2334.
Johnson, M.C., Rutherford, M.J., 1989. Experimental calibration of the aluminium-in-hornblende geobarometer with application to Long Valley caldera (California) volcanic rocks. Geology 17, 837–841.
Klimm, K., Holtz, F., Johannes, W., King, P., 2003. Fractionation of metaluminous A-type granites: an experimental study of the Wangrah Suite, Lachlan Fold Belt, Australia. Precambrian Research 124, 327–341.
Krippner, S.J.P., Briggs, R.M., Wilson, C.J.N., Cole, J.W., 1998. Petrography and geochemistry of lithic fragments in ignimbrites from the Mangakino volcanic centre: implications for the composition of the subvolcanic crust in western Taupo Volcanic Zone, New Zealand. New Zealand Journal of Geology and Geophysics 41, 187–199.
Lange, R.A., Frey, H.M., Hector, J., 2009. A thermodynamic model for the plagioclase-liquid hygrometer/thermometer. American Mineralogist 94, 494–506.
Leake, B.E., Woolley, A.R., Birch, W.D., Burke, E.A., Ferraris, G., Grice, J.D., Hawthorne, F.C., Kisch, H.J., Krivovichev, V.G., Schumacher, J.C., 2004. Nomenclature of amphiboles: additions and revisions to the International Mineralogical Association's amphibole nomenclature. American Mineralogist 89, 883–887.
Lindsay, J.M., Schmitt, A.K., Trumbull, R.B., de Silva, S.L., Siebel, W., Emmermann, R., 2001. Magmatic evolution of the La Pacana caldera system, central Andes, Chile: compositional variation of two cogenetic, large-volume felsic ignimbrites. Journal of Petrology 42, 459–486.
Mahood, G.A., 1990. Second reply to comment of R.S.J. Sparks, H.E. Huppert and C.J.N. Wilson on "Evidence for long residence times of rhyolitic magma in the Long Valley magmatic system: the isotopic record in the precaldera lavas of Glass Mountain". Earth and Planetary Science Letters 99, 395–399.
Marsh, B.D., 1981. On the crystallinity, probability of occurrence, and rheology of lava and magma. Contributions to Mineralogy and Petrology 78, 85–98.
Matthews, N.E., Pyle, D.M., Smith, V.C., Wilson, C.J.N., Huber, C., van Hinsberg, V., 2012a. Quartz zoning and the pre-eruptive evolution of the 340-ka Whakamaru magma systems, New Zealand. Contributions to Mineralogy and Petrology 163, 87–107.
Matthews, N.E., Huber, C., Pyle, D.M., Smith, V.C., 2012b. Timescales of magma recharge and reactivation of large silicic systems from Ti diffusion in quartz. Journal of Petrology 53, 1385–1416.
Maughan, L.L., Christiansen, E.H., Best, M.G., Grommé, C.S., Deino, A.L., Tingey, D.G., 2002. The Oligocene Lund Tuff, Great Basin, USA: a very large volume monotonous intermediate. Journal of Volcanology and Geothermal Research 113, 129–157.
Mortimer, N., 2000. Metamorphic discontinuities in orogenic belts: example of the garnet–biotite–albite zone in the Otago Schist, New Zealand. International Journal of Earth Sciences 89, 295–306.
Murphy, M.D., Sparks, R.S.J., Barclay, J., Carroll, M.R., Brewer, T.S., 2000. Remobilization of andesite magma by intrusion of mafic magma at the Soufriere Hills volcano, Montserrat, West Indies. Journal of Petrology 41, 21–42.
Nelson, S.T., Montana, A., 1992. Sieve-textured plagioclase in volcanic rocks produced by rapid decompression. American Mineralogist 77, 1242–1249.
Pain, C.F., 1975. Some tephra deposits in the south-west Waikato area, North Island, New Zealand. New Zealand Journal of Geology and Geophysics 18, 541–550.
Pallister, J.S., Hoblitt, R.P., Reyes, A.G., 1992. A basalt trigger for the 1991 eruptions of Pinatubo volcano? Nature 356, 426–428.
Petford, N., 2003. Rheology of granitic magmas during ascent and emplacement. Annual Review of Earth and Planetary Sciences 31, 399–427.
Price, R.C., Gamble, J.A., Smith, I.E.M., Stewart, R.B., Eggins, S.M., Wright, I.C., 2005. An integrated model for the temporal evolution of andesites and rhyolites and crustal development in New Zealand's North Island. Journal of Volcanology and Geothermal Research 140, 1–24.
Putirka, K.D., 2005. Igneous thermometers and barometers based on plagioclase + liquid equilibria: tests of some existing models and new calibrations. American Mineralogist 90, 336–346.
Putirka, K.D., 2008. Thermometers and barometers for volcanic systems. Reviews in Mineralogy and Geochemistry 69, 61–120.
Richards, J.P., 2011. High Sr/Y arc magmas and porphyry Cu ± Mo ± Au deposits: just add water. Economic Geology 106, 1075–1081.
Ridolfi, F., Renzulli, A., Puerini, M., 2010. Stability and chemical equilibrium of amphibole in calc-alkaline magmas: an overview, new thermobarometric formulations and application to subduction-related volcanoes. Contributions to Mineralogy and Petrology 160, 45–66.
Rutherford, M.J., Devine, J.D., 1988. The May 18, 1980, eruption of Mount St. Helens 3. Stability and chemistry of amphibole in the magma chamber. Journal of Geophysical Research 93, 11949–11959.
Rutherford, M.J., Devine, J.D., 2003. Magmatic conditions and magma ascent as indicated by hornblende phase equilibria and reactions in the 1995–2002 Soufriere Hills magma. Journal of Petrology 44, 1433–1453.
Sisson, T.W., 1994. Hornblende-melt trace-element partitioning measured by ion microprobe. Chemical Geology 117, 331–344.
Sisson, T.W., Bacon, C.R., 1999. Gas-driven filter pressing in magmas. Geology 27, 613–616.

Sparks, R.S.J., Huppert, H.E., Wilson, C.J.N., 1990. Comment on: "Evidence for long residence times of rhyolitic magma in the Long Valley magmatic system: the isotopic record in pre caldera lavas of Glass Mountain", by A.N. Halliday, G.A. Mahood, P. Holden, J. M. Metz, T.J. Dempster and J.P. Davidson. Earth and Planetary Science Letters 99, 387–389.

Sutton, A.N., Blake, S., Wilson, C.J.N., Charlier, B.L.A., 2000. Late Quaternary evolution of a hyperactive rhyolite magmatic system: Taupo volcanic centre, New Zealand. Journal of the Geological Society, London 157, 537–552.

Vigneresse, J.L., Barbey, P., Cuney, M., 1996. Rheological transitions during partial melting and crystallization with application to felsic magma segregation and transfer. Journal of Petrology 37, 1579–1600.

Wilson, C.J.N., 1986. Reconnaissance stratigraphy and volcanology of ignimbrites from Mangakino volcano. In: Smith, I.E.M. (Ed.), Late Cenozoic Volcanism in New Zealand, Royal Society of New Zealand Bulletin, 23, pp. 179–193.

Wilson, C.J.N., Houghton, B.F., McWilliams, M.O., Lanphere, M.A., Weaver, S.D., Briggs, R.M., 1995. Volcanic and structural evolution of Taupo Volcanic Zone, New Zealand: a review. Journal of Volcanology and Geothermal Research 68, 1–28.

Wilson, C.J.N., Blake, S., Charlier, B.L.A., Sutton, A.N., 2006. The 26.5 ka Oruanui eruption, Taupo volcano, New Zealand: development, characteristics and evacuation of a large rhyolitic magma body. Journal of Petrology 47, 35–69.

Wilson, C.J.N., Charlier, B.L.A., Rowland, J.V., Browne, P.R.L., 2010. U–Pb dating of zircon in subsurface hydrothermally altered pyroclastic deposits and implications for subsidence in a magmatically active rift: Taupo Volcanic Zone, New Zealand. Journal of Volcanology and Geothermal Research 191, 69–78.

Wotzlaw, J.-F., Schaltegger, U., Frick, D.A., Dungan, M.A., Gerdes, A., Gunther, D., 2013. Tracking the evolution of large-volume silicic magma reservoirs from assembly to supereruption. Geology 41, 867–870.